

Quantum oscillations of the quasiparticle lifetime in a metal

<https://doi.org/10.1038/s41586-023-06330-y>

Received: 5 October 2022

Accepted: 15 June 2023

Published online: 2 August 2023

 Check for updates

Nico Huber^{1,5}, Valentin Leeb^{1,2,5}, Andreas Bauer^{1,3}, Georg Benka¹, Johannes Knolle^{1,2,4}✉, Christian Pfleiderer^{1,2,3}✉ & Marc A. Wilde^{1,3}✉

Following nearly a century of research, it remains a puzzle that the low-lying excitations of metals are remarkably well explained by effective single-particle theories of non-interacting bands^{1–4}. The abundance of interactions in real materials raises the question of direct spectroscopic signatures of phenomena beyond effective single-particle, single-band behaviour. Here we report the identification of quantum oscillations (QOs) in the three-dimensional topological semimetal CoSi, which defy the standard description in two fundamental aspects. First, the oscillation frequency corresponds to the difference of semiclassical quasiparticle (QP) orbits of two bands, which are forbidden as half of the trajectory would oppose the Lorentz force. Second, the oscillations exist up to above 50 K, in strong contrast to all other oscillatory components, which vanish below a few kelvin. Our findings are in excellent agreement with generic model calculations of QOs of the QP lifetime (QPL). Because the only precondition for their existence is a nonlinear coupling of at least two electronic orbits, for example, owing to QP scattering on defects or collective excitations, such QOs of the QPL are generic for any metal featuring Landau quantization with several orbits. They are consistent with certain frequencies in topological semimetals^{5–9}, unconventional superconductors^{10,11}, rare-earth compounds^{12–14} and Rashba systems¹⁵, and permit to identify and gauge correlation phenomena, for example, in two-dimensional materials^{16,17} and multiband metals¹⁸.

In metallic systems with a Fermi surface (FS), Landau quantization¹⁹ and the associated QOs²⁰ represent an invaluable spectroscopic demonstration of the single-particle, independent-band character of electronic excitations. Building on the semiclassical approximation of charge-carrier motion in which quantum phases are connected to classical trajectories²¹, Onsager attributed QOs to the formation of cyclotron orbits with a quantized cross-sectional area. Accordingly, the frequency f of the oscillations is related to the extremal area of an orbit in k -space, A_k , through $f = \hbar/(2\pi e)A_k$, in which \hbar is the reduced Planck constant and e is the electron charge^{22,23}. The effects of finite temperatures can be described by an averaging of QOs at zero temperature with a distribution of different Fermi levels as weighted with a probability given by the negative derivative $-dn_{FD}(E)/dE$ of the Fermi–Dirac distribution n_{FD} (ref. 21). As shown by Lifshitz and Kosevich (LK)²⁴, this results in a damping factor of the amplitude of the oscillations, $R_T(m^*) = X/\sinh X$, that depends on the ratio $X = 2\pi^2(k_B T)/(\hbar\omega_c)$ of the thermal energy $k_B T$ to the cyclotron energy $\hbar\omega_c = \hbar eB/m^*$, where k_B is the Boltzmann constant, T is the temperature, B is the magnetic field and ω_c is the cyclotron frequency. Hence, the thermal damping $R_T(m^*)$ is governed by a single-particle effective mass m^* (refs. 25,26), in which multiband metals are treated as a collection of completely independent bands.

Well-known amendments to the LK formalism²¹ comprising quantum tunnelling, quantum interference, magnetic interactions and

chemical-potential oscillations maintain a single-particle character of the oscillation spectra, whereas recent work on QOs in correlated insulators represents an exception^{27–30}. Likewise, interactions that limit the QPL are, so far, also treated on an effective single-particle level. Namely, using a Lorentzian distribution of the Landau-level energies to reflect the exponential decay associated with the relaxation-time approximation, Dingle modelled the decrease of τ owing to interactions in analogy to the LK formalism³¹ in terms of a reduction factor $R_D = \exp(-\pi m/eB\tau)$ with a scattering time τ for a given QP band. This energy distribution is often expressed in terms of the Dingle temperature $T_D \propto 1/\tau$.

However, as reported in our paper, the effects of QP scattering are much richer, causing QOs of the QPL as a direct consequence of the combination of the Landau quantization of the density of states (DOS) with Fermi’s golden rule. The conditions for QOs of the QPL are remarkably simple: they only require some form of nonlinear coupling between FS orbits, that is, scattering from one FS orbit to the other and back. The resulting QO frequency arises in all physical observables, most prominently electrical transport, but without a corresponding FS cross-section. Thus, QOs of the QPL may be expected in any metal featuring Landau quantization and mutually interacting electronic states. Underscoring this general relevance, an analogy exists with so-called magneto-intersubband oscillations in two-dimensional electron gases³² and quasi-two-dimensional metals³³.

¹TUM School of Natural Sciences, Department of Physics, Technical University of Munich, Garching, Germany. ²Munich Center for Quantum Science and Technology (MCQST), Munich, Germany. ³Centre for Quantum Engineering (ZQE), Technical University of Munich, Garching, Germany. ⁴Blackett Laboratory, Imperial College London, London, UK. ⁵These authors contributed equally: Nico Huber, Valentin Leeb. ✉e-mail: j.knolle@tum.de; christian.pfleiderer@tum.de; marc.wilde@tum.de

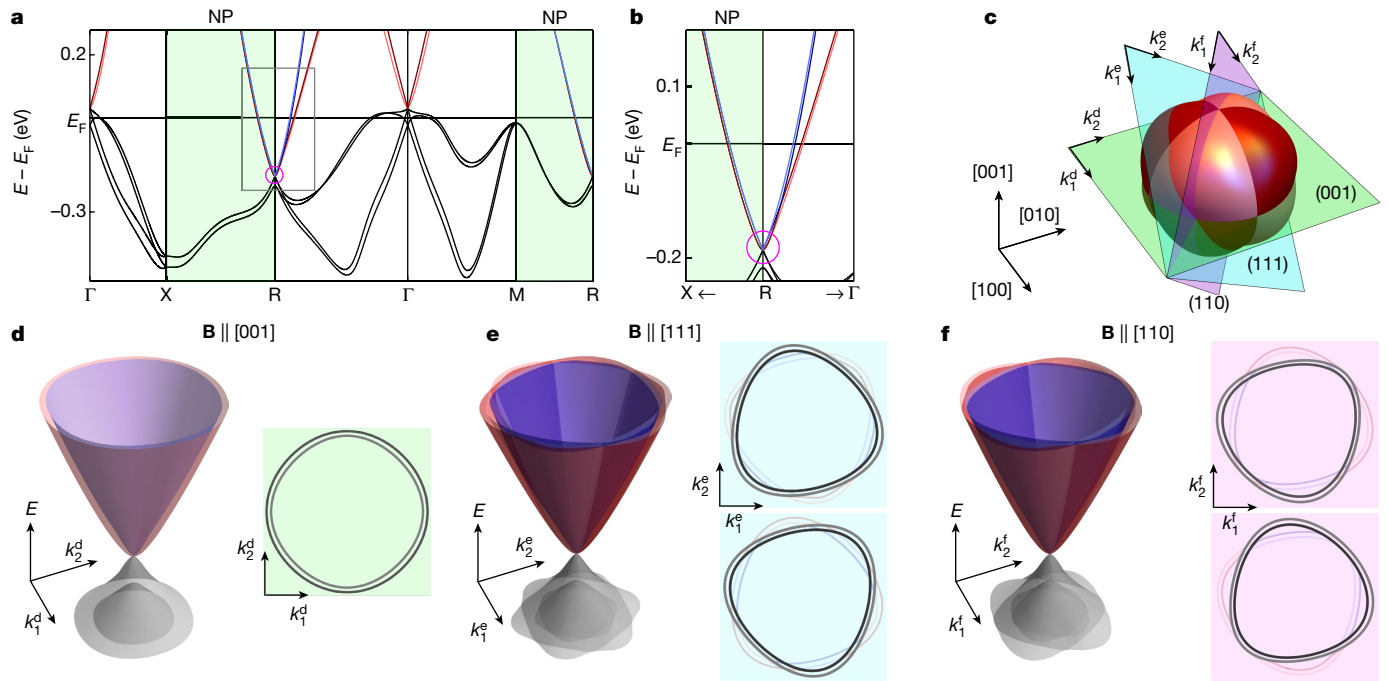


Fig. 1 | Electronic band structure of CoSi and FS orbits featuring QOs of the QPL. For any field direction, only two different extremal FS cross-sectional areas exist around the R point. Topological nodal planes (denoted by ‘NP’) are shown in green shading. See also Extended Data Fig. 1 for details why effectively two FS orbits dominate the spectra. **a**, Electronic band structure of CoSi. **b**, Multifold band crossings (circled) and nested dispersion near E_F in the vicinity of the intersection of three topological nodal planes at the R point. **c**, FS pockets around the R point. Four nearly spherical FS sheets intersect at

the nodal planes. Planes of extremal orbits for selected field directions as shown in panels **d**–**f** are denoted by different colour shading. Directions in momentum space spanning these planes are denoted with a superscript referring to panels **d**, **e** and **f**. **d**, Dispersion for $\mathbf{B} \parallel [001]$ (left) and FS orbits as seen in the direction of the applied field (right, grey lines). The FS orbits reside within a nodal plane. **e**, Dispersion for $\mathbf{B} \parallel [111]$ (left) and FS orbits as seen in the direction of the applied field (right, coloured lines). **f**, As in panels **d** and **e** for $\mathbf{B} \parallel [110]$. In all cases, the cross-sectional areas are pairwise degenerate.

Band topology of CoSi

For our study, we selected CoSi, a three-dimensional system far from electronic instabilities with a well-defined FS and vanishingly small exchange-enhanced spin splitting. Crystallizing in the chiral space group 198, a comprehensive theoretical assessment recently established a network of topological nodal planes, multifold degeneracies and Weyl points³⁴ (Methods). Shown in Fig. 1a is the calculated electronic structure taking into account spin-orbit coupling, in which the presence of nodal planes (green shading) on the surface of the cubic Brillouin zone, as well as a sixfold degenerate point at R, are highlighted^{18,35}. Key for our study are the extremely simple QO spectra associated with the R point of the Brillouin zone^{34,36}. Whereas four almost parallel bands originate from the sixfold degeneracy at R (Fig. 1b), thus forming four small intersecting electron pockets (Fig. 1c), only two dominant frequencies characteristic of two FS orbits are observed for all field orientations. This may be traced to exact degeneracies enforced by the nodal planes at the R point and further quasi-degeneracies, being well described in terms of two adjacent FS orbits.

For instance, for $\mathbf{B} \parallel [001]$, the dispersion in the plane of the extremal orbits (green) corresponds to two wine goblet shapes that are twofold degenerate everywhere (left-hand side of Fig. 1d). The associated extremal orbits at the FS are here given by two concentric rings (grey lines on the right-hand side of Fig. 1d). The same is effectively true for \mathbf{B} away from $\mathbf{B} \parallel [001]$, as illustrated for $\mathbf{B} \parallel [111]$ and $\mathbf{B} \parallel [110]$ in Fig. 1e,f. Although the FS contours (coloured lines) seem more complicated, the degeneracies enforced by the nodal planes and the extra quasi-degeneracies result in four orbits with pairwise identical cross-sections. In a recent study, it has been proposed that the QO spectra at the R point are because of hidden quasi-symmetries³⁶, resulting in the same four orbits with pairwise identical cross-sections (see also Extended Data Fig. 1).

Shubnikov-de Haas oscillations

Shown in Fig. 2a are the transverse magnetoresistance, ρ_{xx} , and the Hall resistivity, ρ_{xy} , at 20 mK (Methods). Both ρ_{xx} and ρ_{xy} exhibit pronounced oscillations for magnetic fields exceeding about 6 T. Subtracting a monotonic background, the oscillatory signal components, $\tilde{\rho}_{xx}$ and $\tilde{\rho}_{xy}$, were found to show the same QO spectra (Fig. 2b and Methods). Periodic in $1/B$, a pronounced beating pattern characteristic of two nearly identical frequencies dominates the data. Typical fast Fourier transforms (FFTs) for magnetic field parallel to [001] are shown in Fig. 2c. Two prominent peaks at $f_\alpha = 565$ T and $f_\beta = 663$ T with up to three higher harmonics may be resolved owing to FS sheets centred on the R point^{34,36} (Methods). In the following, we focus on $\tilde{\rho}_{xx}$; $\tilde{\rho}_{xy}$ is presented in Extended Data Fig. 2.

Not reported previously are the two further frequencies shown in Fig. 2d,e, which correspond to the difference, $f_{\beta-\alpha}$, and the sum, $f_{\beta+\alpha}$, of the fundamental frequencies f_α and f_β . As a function of field direction, a small but unambiguous angle dependence may be discerned for $f_{\beta+\alpha}$, f_β , f_α and $f_{\beta-\alpha}$, as shown in Fig. 2f–i, in which the variations of f_β and f_α agree with the FS calculated in density function theory (DFT)³⁴. Notably, the magnitude of the variations of f_β and f_α differs quantitatively by almost a factor of two, amounting to 9 and 5 T, respectively. This implies a distinct quantitative difference of the angle dependence of the calculated sum and difference of f_β and f_α , in excellent agreement with experiment, and shows that $f_{\beta-\alpha}$ and $f_{\beta+\alpha}$ originate in the difference and the sum of f_α and f_β (see Extended Data Fig. 3 and Methods).

The magnetic-field dependence of f_α and f_β corresponds to Dingle temperatures of $T_{D\alpha,B} \approx 1.3$ K and $T_{D\beta,B} \approx 1.2$ K. The associated QPLs are on the order of $t_{QP} \approx 10^{-12}$ s with a Fermi velocity $v_F \approx 3.4 \times 10^5$ m s⁻¹, consistent with the literature³⁶. In turn, the mean free path is $l \approx 3.4 \times 10^{-7}$ m, characteristic of a tiny defect concentration. Unfortunately, independent

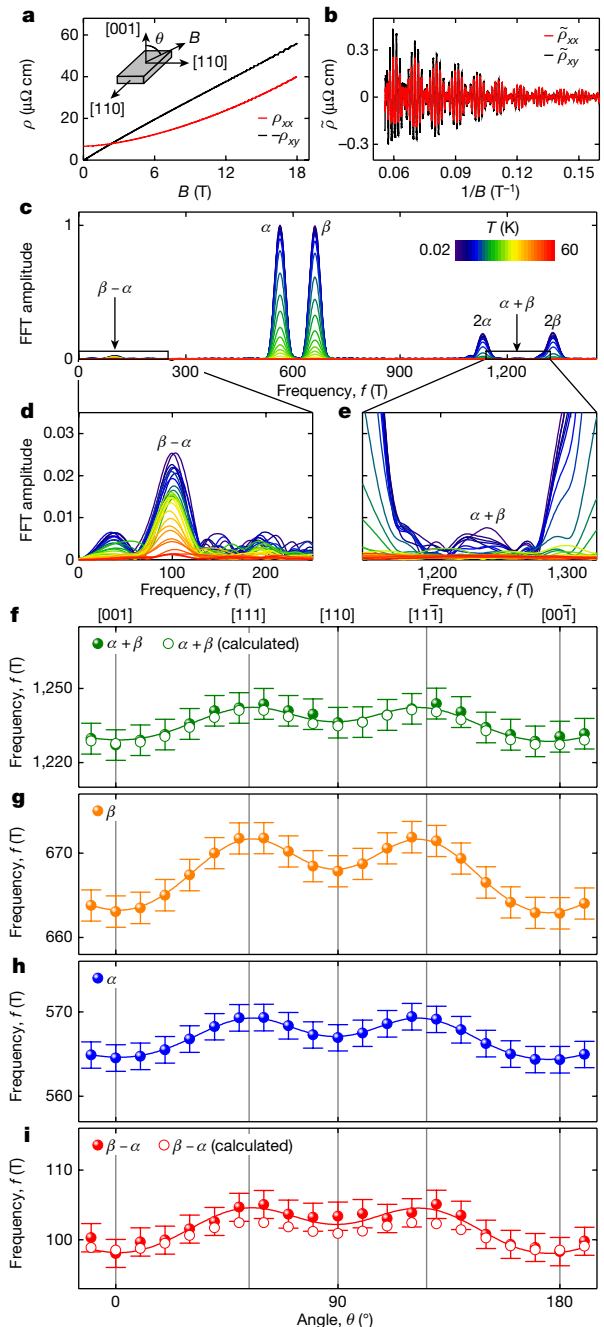


Fig. 2 | QO spectrum of CoSi associated with the R point. **a**, Transverse magnetoresistivity, ρ_{xx} , and Hall resistivity, ρ_{xy} , as a function of magnetic field, B , at $T = 20$ mK and $\theta = 0^\circ$. The inset shows the experimental geometry, in which \mathbf{B} is rotated in the (110) plane and θ denotes the angle between [001] and \mathbf{B} . **b**, Oscillatory signal components of ρ_{xx} and ρ_{xy} after subtraction of a smooth, non-oscillatory background as a function of inverse magnetic field. **c**, Typical FFT spectra of the data shown in panel **b** in the temperature range between $T = 20$ mK and 60 K. **d,e**, Close-up views of the frequency regime of the difference (**d**) and the sum (**e**) of the fundamental frequencies α and β . **f–i**, Oscillation frequencies as a function of θ at $T = 300$ mK. Open circles denote the calculated sum and difference of the frequencies f_α and f_β . The angular dependence further establishes the identification of the detected frequencies $f_{\alpha+\beta}$ (**f**) and $f_{\beta-\alpha}$ (**i**) as combinations of the fundamental frequencies f_α (**h**) and f_β (**g**).

microscopic determination of the precise nature and concentration of defects at these low levels is not possible, posing a substantial challenge in condensed-matter physics on the whole.

Temperature dependence

As shown in Fig. 3a, with increasing temperature, the oscillations at f_α and f_β vanish, whereas the oscillations at $f_{\beta-\alpha}$ may be discerned up to at least 50 K. The agreement between the beating pattern in f_α and f_β at low temperatures with the phase of the oscillations at $f_{\beta-\alpha}$ at elevated temperatures (see Extended Data Figs. 2 and 4) corroborates that $f_{\beta-\alpha}$ and $f_{\alpha+\beta}$ originate in f_α and f_β . Shown in Fig. 3b–d is the temperature dependence of the oscillation amplitude at f_α , f_β , $f_{\beta-\alpha}$ and $f_{\alpha+\beta}$ as normalized to the amplitude of f_α for $T \rightarrow 0$. The small size of the amplitudes at $f_{\beta-\alpha}$ and $f_{\alpha+\beta}$ underscores the high signal-to-noise ratio of our experimental setup.

The temperature dependence of f_α and f_β follows accurately the standard LK formalism, for which we find cyclotron masses of $m_\alpha^* = (0.92 \pm 0.01)m_e$ and $m_\beta^* = (0.96 \pm 0.01)m_e$, respectively, consistent with previous reports^{34,36} (Methods). The presence of $f_{\beta-\alpha}$ up to at least approximately 50 K shown in Fig. 3c is highly unusual. Fitting the temperature dependence between 2 and 60 K yields an effective mass $m_{\beta-\alpha}^* = (0.06 \pm 0.01)m_e$, consistent with $m_\beta^* - m_\alpha^*$. Finally, the amplitude of $f_{\alpha+\beta}$, shown in Fig. 3d, is consistent with $m_{\alpha+\beta}^* = (1.9 \pm 0.3)m_e$.

In comparison with $\tilde{\rho}_{xx}$, the oscillations at $f_{\beta-\alpha}$ observed in $\tilde{\rho}_{xy}$, shown in Extended Data Fig. 2, are characteristic of $m_{HT}^* = (0.07 \pm 0.01)m_e$ (denoted HT). Notably, the temperature dependence suggests a further contribution at low temperatures (denoted LT), consistent either with a decay $R_T(m_\alpha^*)R_T(m_\beta^*)$ or with $R_T(m_{LT}^*)$ and $m_{LT}^* = (1.6 \pm 0.3)m_e \approx m_\beta^* + m_\alpha^*$.

Theoretical model

Our main new findings to be explained theoretically are as follows. First, we observe oscillations at $f_{\beta-\alpha} = f_\beta - f_\alpha$ and $f_{\alpha+\beta} = f_\alpha + f_\beta$ of the frequencies f_α and f_β . Second, as a function of field orientation, tiny variations of $f_{\alpha+\beta}$ and $f_{\beta-\alpha}$ closely track the values calculated from f_α and f_β . Third, as a function of temperature, the FFT amplitudes of f_α and f_β decrease, characteristic of nearly identical masses $m_\alpha^* = (0.92 \pm 0.01)m_e$ and $m_\beta^* = (0.96 \pm 0.01)m_e$, respectively. Fourth, as a function of temperature, the FFT amplitude of $f_{\beta-\alpha}$ survives up to unusually high temperatures, in agreement with $m_\beta^* - m_\alpha^*$, whereas the FFT amplitude of $f_{\alpha+\beta}$ vanishes at much lower temperatures, consistent with $m_\beta^* + m_\alpha^*$. Fifth, the phase of the beating pattern of f_α and f_β at low temperatures is fixed with respect to the phase of $f_{\beta-\alpha}$ at high temperatures.

The properties of CoSi rule out conventional mechanisms as an account of the new oscillation frequencies (see Methods for details)^{21,37,38}. Namely, for magnetic breakdown (MB)^{39–41}, the electron-like FS orbits would require a motion against the Lorentz force for half of the trajectory associated with $f_\beta - f_\alpha$, the amplitude of which would be suppressed much faster with increasing temperature. Chemical-potential oscillations are well known in two-dimensional systems but will be quantitatively irrelevant for the nearly isotropic three-dimensional FS sheets of CoSi. For magnetic interactions, the values of $d\bar{M}/dH$ are orders of magnitude too small to account for our experiment (see Extended Data Fig. 5). Finally, quantum interference would require a superposition between different pathways connected by MB junctions^{42,43}, which do not exist for $\mathbf{B} \parallel [001]$ (Fig. 1d) and do not have suitable MB probabilities for other field directions (Extended Data Fig. 1).

Instead, our findings can be explained in terms of QOs of the QPL, as summarized in Fig. 4, in which the single precondition is some form of nonlinear coupling that generates intraorbit and interorbit transitions, as illustrated in Fig. 4a. To demonstrate the plausibility of the nonlinear coupling for a specific microscopic situation, we considered defect scattering (see Methods). A well-known consequence of QP transitions is a broadening of the Landau levels as depicted in Fig. 4b, in which the inverse of the QPL $1/\tau$ corresponds to the half-width of the DOS peaks. Assuming the Born approximation and Fermi's golden rule, the QPL varies with the DOS at E_F . Hence, as a function of magnetic field, τ includes an oscillatory component as well as the average value.

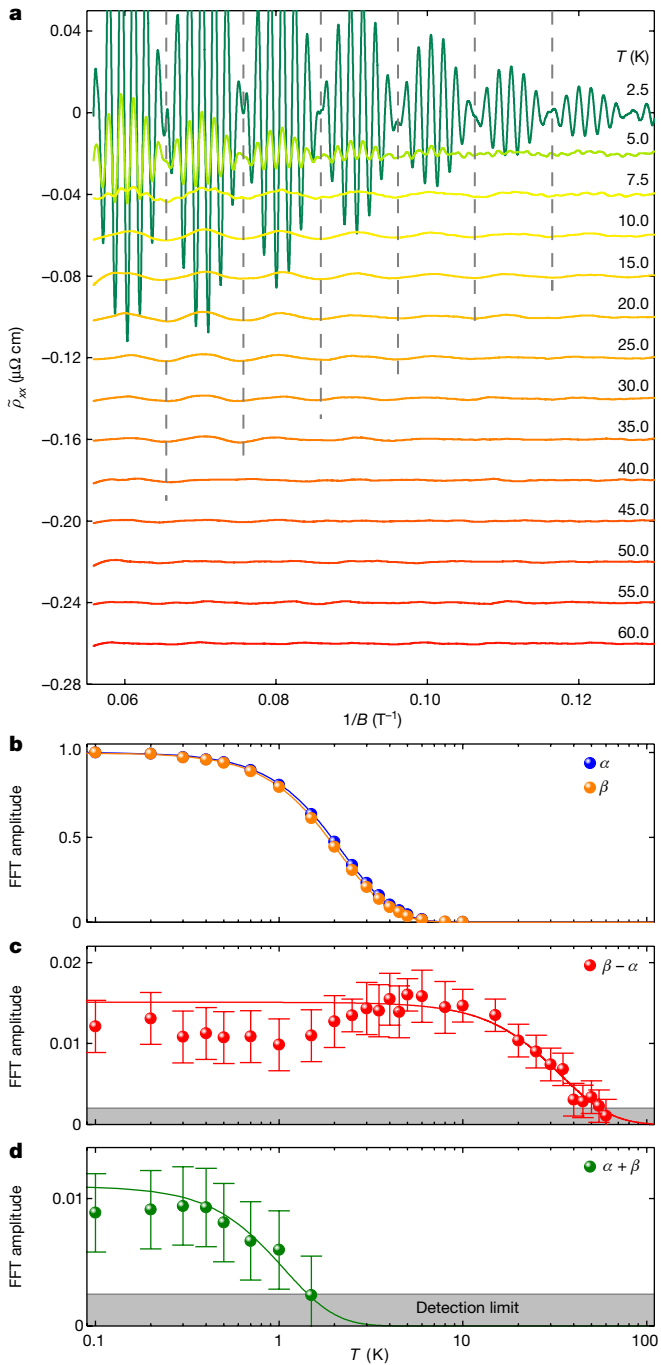


Fig. 3 | Temperature dependence of Shubnikov–de Haas oscillations in the transverse magnetoresistance of CoSi. Oscillation amplitudes shown in panels **b–d** were analysed in the magnetic field range between 9 and 18 T with **B** applied along the [001] direction and normalized to the amplitude of f_α at $T = 20$ mK. **a**, Oscillatory component of ρ_{xx} as a function of inverse magnetic field at different temperatures. Curves are shifted for better visibility. **b**, Oscillation amplitudes of f_α and f_β as a function of temperature T . Lines represent a fit of the temperature reduction factor R_T in the LK formalism. The inferred effective masses are $m_\alpha^* = (0.92 \pm 0.01)m_e$ and $m_\beta^* = (0.96 \pm 0.01)m_e$, in good agreement with the effective masses obtained from ρ_{xy} (Extended Data Fig. 2). Error bars are smaller than the data points. **c**, Oscillation amplitudes of the difference frequency $f_{\beta-\alpha}$. A fit of the data between 2 and 60 K with the LK temperature reduction factor R_T is represented by the red line and yields an effective mass of $m_{\beta-\alpha}^* = (0.06 \pm 0.01)m_e$. **d**, Oscillation amplitudes of frequency $f_{\alpha+\beta}$. The line represents a LK fit yielding an effective mass of $m_{\alpha+\beta}^* = (1.9 \pm 0.4)m_e$.

In the presence of intraorbit scattering, the oscillatory component of τ varies with the cyclotron frequency of the underlying FS orbit, as shown in Fig. 4c. Remarkably, in the presence of intraorbit and interorbit transitions, τ oscillates with both frequencies of the participating FS orbits, f_α and f_β , as depicted in Fig. 4d, in which the intraorbit and interorbit oscillations were assumed to be equally strong. Expressed in terms of the Dingle temperature associated with the QPL, T_D , and the Dingle temperature of the non-oscillatory average, T_D^0 , the inverse of the QPL may be written as

$$\frac{1}{\tau} \propto T_D \propto T_D^0 + A_\alpha \cos\left(\frac{2\pi f_\alpha}{B}\right) + A_\beta \cos\left(\frac{2\pi f_\beta}{B}\right) \quad (1)$$

in which A_α and A_β are prefactors and B is the magnetic field.

In the physical quantities studied experimentally, the QOs of the QPL cause further oscillatory components expressed conveniently in terms of T_D . Owing to a further linear dependence on T_D , the effect is particularly pronounced in the electrical-transport properties

$$\sigma \propto T_D \left[\cos\left(\frac{2\pi f_\alpha}{B}\right) + \cos\left(\frac{2\pi f_\beta}{B}\right) \right] R_D(T_D). \quad (2)$$

For the sake of the argument, it is not necessary to distinguish between $\tilde{\rho}_{xx}$ and $\tilde{\rho}_{xy}$ here. Inserting T_D , we obtain, to leading order, terms in $\cos(2\pi f_\alpha/B) \times \cos(2\pi f_\beta/B)$ and $\cos^2(2\pi f_\lambda/B)$ ($\lambda = \alpha, \beta$). Using trigonometric addition theorems, the former decomposes into $\cos(2\pi(f_\beta - f_\alpha)/B)$ and $\cos(2\pi(f_\beta + f_\alpha)/B)$. Hence, the combined effect of intraorbit and interorbit transitions accounts naturally for the nearly isotropic oscillatory components at $f_\beta - f_\alpha$ and $f_\alpha + f_\beta$ observed experimentally. Moreover, it explains naturally the fixed phase relationship of $f_\beta - f_\alpha$ with f_α and f_β observed experimentally (Extended Data Fig. 4). Further subleading oscillatory dependencies that we ignore for clarity, such as $2f_\alpha - f_\beta$, $2f_\beta - f_\alpha$, $2f_\beta - 2f_\alpha$, $3f_\beta - f_\alpha$, $2f_\alpha - 2f_\beta$, $3f_\alpha$ and so forth, arise from the Dingle damping factor itself, $R_D(T_D)$ (see Methods). As for the terms in $\cos^2(2\pi f_\lambda/B)$ ($\lambda = 1, 2$), which are purely because of intraorbit transitions, these will only modify the higher harmonics of the fundamental frequencies.

It is now instructive to address the effects of finite temperatures as illustrated in Fig. 4e. The fundamental QO frequencies are determined by the extremal cross-sectional areas $A_k(E_F)$. Accordingly, oscillations at $f_\beta - f_\alpha$ and $f_\alpha + f_\beta$ also change as a function of E_F . Recalling that $R_T(T)$ originates from an averaging of orbits with different E_F , weighted by $-dn_{FD}/dE$, we find that the width of the distribution of Fermi levels at finite temperature, $\delta E_F \approx k_B T$, causes a distribution of frequencies, δf , that scales with the cyclotron mass, $\delta f/k_B T = \hbar/(2\pi e)\partial A_\lambda/\partial E = m/(e\hbar)$. Consequently, for the oscillations at $f_\beta - f_\alpha$ and $f_\alpha + f_\beta$, finite temperatures cause distributions given by $\delta(f_\beta - f_\alpha)/k_B T = \hbar/(2\pi e)\partial(A_{\alpha,\beta} - A_{\alpha,\alpha})/\partial E = (m_\beta - m_\alpha)/(e\hbar)$ and $\delta(f_\alpha + f_\beta)/k_B T = (m_\beta + m_\alpha)/(e\hbar)$, respectively. Taken together, this explains the unusual temperature dependence of the oscillation amplitudes $f_\beta - f_\alpha$ and $f_\alpha + f_\beta$ compared with f_α and f_β .

QOs of the QPL are generic and may be expected for any FS orbits coupled nonlinearly regardless of the coupling mechanism and the specific orbits involved. Thus, they may be intrinsic in perfectly pure systems, arising, for example, from interactions with collective excitations. In case the nonlinear coupling is because of defects, a sweet spot of the concentration is expected at which intraorbit scattering is sufficiently weak such that Landau quantization persists, whereas interorbit scattering is sufficiently strong to couple the bands. In real materials, the same microscopic defects may give rise to both intraorbit and interorbit transitions.

It is also instructive to consider the implications of different band dispersions (see also Extended Data Fig. 6). For instance, if the cyclotron masses of f_α and f_β are equal over an energy range on the order $k_B T$ around E_F regardless of the full-dispersion relation, a complete

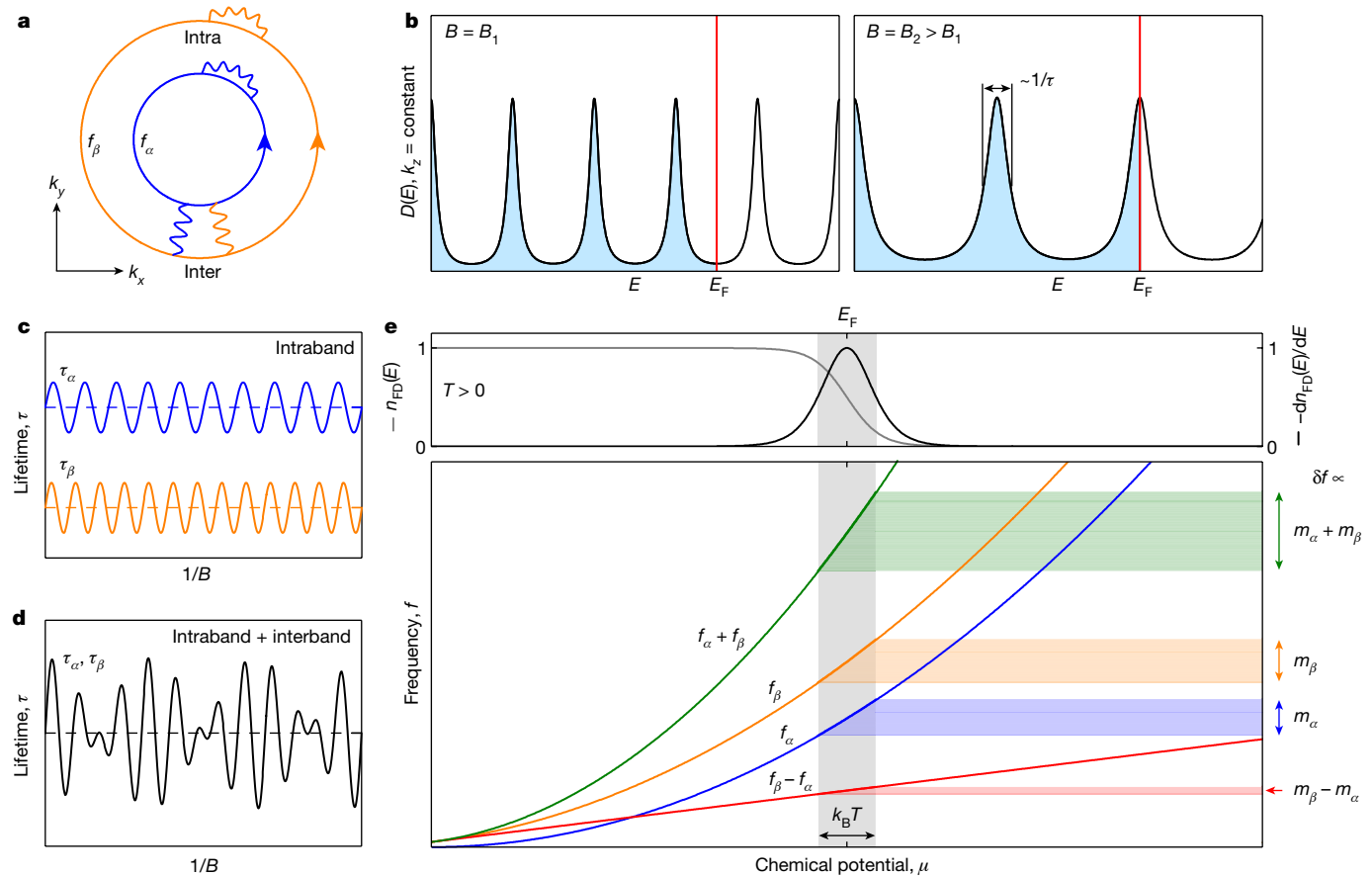


Fig. 4 | Origin of QOs of the QPL. **a**, Depiction of two FS orbits arising from nested bands. Associated with the two FS orbits are two oscillation frequencies f_α and f_β . Intraband scattering causes transitions within each FS orbit; interband scattering causes transitions between the FS orbits. The scattering effectively mixes the orbits. For the associated Feynman diagrams, see Methods. **b**, DOS, $D(E)$, owing to Landau quantization of cyclotron orbits under magnetic fields B_1 and $B_2 > B_1$. The Landau-level separation and degeneracy varies linearly with B such that the DOS at the Fermi energy E_F is an oscillatory function of $1/B$. Intraband transitions cause a broadening of the Landau levels. As the lifetime τ of the cyclotron orbits varies with $D(E_F)$, it is also an oscillatory function of $1/B$. **c**, QPL associated with FS orbits α and β with intraorbit but no interorbit

scattering. **d**, QPL associated with FS orbits α and β in the presence of intraorbit and interorbit scattering. As the interorbit scattering depends on the DOS on both FS orbits α and β , the QPL oscillates with a superposition of the densities of states on both orbits. **e**, Connection between the temperature dependence of the oscillation amplitude and the effective mass as proposed by Lifshitz and Kosevich. The nearly parallel dispersion of the orbits α and β as a function of energy near the chemical potential results in a nearly complete suppression (doubling) of the dispersion for oscillations at $f_{\beta-\alpha}$ ($f_{\alpha+\beta}$). The temperature dependence is governed by the variation of frequency δf in an interval $k_B T$ around E_F depicted in grey shading given by the negative of the derivative of the Fermi distribution with respect to energy, $-dn_{FD}(E)/dE$.

suppression of the temperature decay is expected. Such a behaviour may be erroneously taken as evidence of fermions with vanishing cyclotron mass. The further enhancement of the oscillation amplitude of $f_{\beta-\alpha}$ below about 1 K, seen in $\tilde{\rho}_{xy}$ (Extended Data Fig. 2), may be because of other coupling mechanisms, such as Coulomb repulsion, as recently discussed for quasi-two-dimensional systems³⁸. Notably, all of these mechanisms predict a strong temperature dependence^{21,38}, that is, $R_T(m_\alpha^*)R_T(m_\beta^*)$, which is inherently different to our theory.

As stated above, QOs of the QPL are particularly pronounced in the transport properties owing to the further dependence on the QPL. In turn, similar QO frequencies, albeit with a different amplitude and temperature dependence, are also expected in the magnetization, notably the de Haas–van Alphen effect, as well as all other physical quantities. Thus, differences in the spectral weight of QOs observed in different physical quantities will permit to identify QOs of the QPL.

Discussion

QOs of the QPL are generic for any FS orbits coupled nonlinearly. They may be identified most easily for the two electron-like FS sheets in CoSi. Such interband QOs of the QPL may also be expected for

electron-like and hole-like FS sheets. Indeed, a sum frequency between an electron-like and a hole-like FS sheet has been reported in $\text{Co}_3\text{Sn}_2\text{S}_2$, HfSiS and UTe₂, in which they would resolve the inconsistencies with conventional mechanisms, as noted in several papers^{5,7,9}. Similarly, QO of the QPL may also arise in anisotropic single-band systems between orbits on different extremal cross-sections on the same FS sheet. Such intraband QOs of the QPL may have been observed unknowingly in MoSi₂ and WSi₂ (ref. 8), in which disagreement of a difference frequency with conventional mechanisms was emphasized. Further, efforts to identify QO frequencies that are not present in DFT have motivated proposals of FS reconstructions. However, QO of the QPL may allow to reconcile some QO spectra without the need for FS reconstructions. Examples may exist in the FeAs or kagome superconductors^{10,17,44}. Indeed, one might even reassess the cuprate superconductors, representing single-band systems¹¹. Similarly, in heavy-fermion compounds, unexplained QOs with moderately heavy masses may be because of FS orbits with very heavy masses that evade detection down to the low-mK regime^{4,12–14}.

QOs of the QPL may be also of great relevance in spin-orbit coupled systems with Rashba-type or Dresselhaus-type dispersions or—in general—for nested FS pockets that enclose (near) degeneracies of two or more

bands. In bulk multivalley systems, QOs of the QPL may arise from FS pockets not centred around a common momentum vector in the presence of large-momentum transitions, for example, mediated by spin, charge or phonon fluctuations⁴⁵. This will help to construct more accurate models of quantum materials and may lead to applications in, for example, valleytronics. Taken together, QOs of the QPL generally allow to quantify the strength of QP scattering in bulk and tailored materials, as reported recently in twisted bilayer graphene^{16,17}.

Online content

Any methods, additional references, Nature Portfolio reporting summaries, source data, extended data, supplementary information, acknowledgements, peer review information; details of author contributions and competing interests; and statements of data and code availability are available at <https://doi.org/10.1038/s41586-023-06330-y>.

1. Luttinger, J. M. Theory of the de Haas-van Alphen effect for a system of interacting fermions. *Phys. Rev.* **121**, 1251–1258 (1961).
2. Engelsberg, S. & Simpson, G. Influence of electron-phonon interactions on the de Haas-van Alphen effect. *Phys. Rev. B* **2**, 1657–1665 (1970).
3. Wasserman, A., Springford, M. & Hewson, A. Theory of the de Haas-van Alphen effect for heavy-fermion alloys. *J. Phys. Condens. Matter* **1**, 2669–2676 (1989).
4. Taillefer, L., Newbury, R., Lonzarich, G., Fisk, Z. & Smith, J. Direct observation of heavy quasiparticles in UPt₃ via the dHvA effect. *J. Mag. Mag. Mater.* **63–64**, 372–376 (1987).
5. van Delft, M. R. et al. Electron-hole tunneling revealed by quantum oscillations in the nodal-line semimetal HfSiS. *Phys. Rev. Lett.* **121**, 256602 (2018).
6. Müller, C. S. A. et al. Determination of the Fermi surface and field-induced quasiparticle tunneling around the Dirac nodal loop in ZrSiS. *Phys. Rev. Res.* **2**, 023217 (2020).
7. Ding, L. et al. Quantum oscillations, magnetic breakdown and thermal Hall effect in Co₃Sn₂S₂. *J. Phys. D Appl. Phys.* **54**, 454003 (2021).
8. Pavlosiuk, O., Swatek, P. W., Wang, J.-P., Wiśniewski, P. & Kaczorowski, D. Giant magnetoresistance, Fermi-surface topology, Shoenberg effect, and vanishing quantum oscillations in the type-II Dirac semimetal candidates MoSi₂ and WSi₂. *Phys. Rev. B* **105**, 075141 (2022).
9. Broyles, C. et al. Revealing a 3D Fermi surface and electron-hole tunneling in UTe₂ with quantum oscillations. Preprint at <https://arxiv.org/abs/2303.09050> (2023).
10. Reiss, P. et al. Quenched nematic criticality and two superconducting domes in an iron-based superconductor. *Nat. Phys.* **16**, 89–94 (2020).
11. Sebastian, S. E. & Proust, C. Quantum oscillations in hole-doped cuprates. *Annu. Rev. Condens. Matter Phys.* **6**, 411–430 (2015).
12. McMullan, G. J. et al. The Fermi surface and f-valence electron count of UPt₃. *New J. Phys.* **10**, 053029 (2008).
13. Shishido, H. et al. Anomalous change in the de Haas–van Alphen oscillations of CeCoIn₅ at ultralow temperatures. *Phys. Rev. Lett.* **120**, 177201 (2018).
14. Dalgaard, K. J., Lei, S., Wiedmann, S., Bremholm, M. & Schoop, L. M. Anomalous Shubnikov-de Haas quantum oscillations in rare-earth tritelluride NdTe₃. *Phys. Rev. B* **102**, 245109 (2020).
15. Sunko, V. et al. Maximal Rashba-like spin splitting via kinetic-energy-coupled inversion-symmetry breaking. *Nature* **549**, 492–496 (2017).
16. Phinney, I. et al. Strong intertervalley scattering in twisted bilayer graphene revealed by high-temperature magneto-oscillations. *Phys. Rev. Lett.* **127**, 056802 (2021).
17. Broyles, C. et al. Effect of the interlayer ordering on the Fermi surface of Kagome superconductor CsV₃Sb₅ revealed by quantum oscillations. *Phys. Rev. Lett.* **129**, 157001 (2022).
18. Sanchez, D. S. et al. Topological chiral crystals with helicoid-arc quantum states. *Nature* **567**, 500–505 (2019).
19. Landau, L. Diamagnetismus der Metalle. *Z. Phys.* **64**, 629–637 (1930).
20. de Haas, W. J. & van Alphen, P. M. The dependence of the susceptibility of diamagnetic metals upon the field. *Proc. Netherlands Roy. Acad. Sci.* **33**, 1106–1118 (1930).
21. Shoenberg, D. *Magnetic Oscillations in Metals* (Cambridge Univ. Press, 1984).
22. Peierls, R. Zur Theorie des Diamagnetismus von Leitungselektronen. *Z. Phys.* **80**, 763–791 (1933).
23. Onsager, L. Interpretation of the de Haas-van Alphen effect. *Lond. Edinb. Dublin Philos. Mag. J. Sci.* **43**, 1006–1008 (1952).
24. Lifshitz, I. M. & Kosevich, A. Theory of magnetic susceptibility in metals at low temperatures. *Sov. Phys. JETP* **2**, 636–645 (1956).
25. Kartsovnik, M. V. High magnetic fields: a tool for studying electronic properties of layered organic metals. *Chem. Rev.* **104**, 5737–5781 (2004).
26. Julian, S. R. in *Strongly Correlated Systems* (eds Avella, A. & Mancini, F.) 137–172 (Springer, 2015).
27. Tan, B. S. et al. Unconventional Fermi surface in an insulating state. *Science* **349**, 287–290 (2015).
28. Han, Z., Li, T., Zhang, L., Sullivan, G. & Du, R.-R. Anomalous conductance oscillations in the hybridization gap of InAs/GaSb quantum wells. *Phys. Rev. Lett.* **123**, 126803 (2019).
29. Knolle, J. & Cooper, N. R. Quantum oscillations without a Fermi surface and the anomalous de Haas–van Alphen effect. *Phys. Rev. Lett.* **115**, 146401 (2015).
30. Sodemann, I., Chowdhury, D. & Senthil, T. Quantum oscillations in insulators with neutral Fermi surfaces. *Phys. Rev. B* **97**, 045152 (2018).
31. Dingle, R. B. Some magnetic properties of metals II. The influence of collisions on the magnetic behaviour of large systems. *Proc. R. Soc. Lond. A Math. Phys. Sci.* **211**, 517–525 (1952).
32. Polyanovsky, V. Magnetointersubband oscillations of conductivity in a two-dimensional electronic system. *Sov. Phys. Semicond.* **22**, 1408–1409 (1988).
33. Polyanovsky, V. High-temperature quantum oscillations of the magnetoresistance in layered systems. *Phys. Rev. B* **47**, 1985–1990 (1993).
34. Huber, N. et al. Network of topological nodal planes, multifold degeneracies, and Weyl points in CoSi. *Phys. Rev. Lett.* **129**, 026401 (2022).
35. Rao, Z. et al. Observation of unconventional chiral fermions with long Fermi arcs in CoSi. *Nature* **567**, 496–499 (2019).
36. Guo, C. et al. Quasi-symmetry-protected topology in a semi-metal. *Nat. Phys.* **18**, 813–818 (2022).
37. Alexandrov, A. S. & Kabanov, V. V. Combination quantum oscillations in canonical single-band Fermi liquids. *Phys. Rev. B* **76**, 233101 (2007).
38. Allocca, A. A. & Cooper, N. R. Low-frequency quantum oscillations from interactions in layered metals. *Phys. Rev. Res.* **3**, L042009 (2021).
39. Cohen, M. H. & Falicov, L. M. Magnetic breakdown in crystals. *Phys. Rev. Lett.* **7**, 231–233 (1961).
40. Blount, E. I. Bloch electrons in a magnetic field. *Phys. Rev.* **126**, 1636–1653 (1962).
41. Chambers, R. G. Magnetic breakdown in real metals. *Proc. Phys. Soc.* **88**, 701–715 (1966).
42. Bergmann, G. Weak localization in thin films: a time-of-flight experiment with conduction electrons. *Phys. Rep.* **107**, 1–58 (1984).
43. Lee, P. A. & Stone, A. D. Universal conductance fluctuations in metals. *Phys. Rev. Lett.* **55**, 1622–1625 (1985).
44. Fu, Y. et al. Quantum transport evidence of topological band structures of Kagome superconductor CsV₃Sb₅. *Phys. Rev. Lett.* **127**, 207002 (2021).
45. Allocca, A. A. & Cooper, N. R. Fluctuation-dominated quantum oscillations in excitonic insulators. Preprint at <https://arxiv.org/abs/2302.06633> (2023).

Publisher's note Springer Nature remains neutral with regard to jurisdictional claims in published maps and institutional affiliations.

Springer Nature or its licensor (e.g. a society or other partner) holds exclusive rights to this article under a publishing agreement with the author(s) or other rightsholder(s); author self-archiving of the accepted manuscript version of this article is solely governed by the terms of such publishing agreement and applicable law.

© The Author(s), under exclusive licence to Springer Nature Limited 2023

Article

Methods

Experimental methods and data analysis

Several studies have been reported in the literature that addressed the electronic structure of CoSi (refs. 34–36, 46–50). Our experimental results are in excellent agreement with the literature, when comparison is possible.

Crystal growth and sample preparation. Several single crystals of CoSi were prepared by either optical float zoning^{51,52} or flux growth using Te as flux. The sample investigated most extensively, of which data are reported in this manuscript, was grown by optical float zoning. The ingot was oriented by X-ray Laue diffraction. Using a wire saw, a platelet was cut, with dimensions $2.1 \times 1.0 \times 0.2 \text{ mm}^3$, with faces perpendicular to [110], [110] and [001], respectively. The platelet was subsequently annealed under Ar atmosphere at 1,100 °C for 100 h to improve the sample purity. High sample quality was confirmed by means of the electrical resistivity, magnetization, specific heat and X-ray scattering. The residual resistivity ratio of this sample was 16. Selected measurements of further samples featuring residual resistivity ratios up to 32 confirmed all of the observations reported here. No dependence of the QO of the QPL on the relatively small variations of the residual resistivity ratios in our samples was observed.

Shubnikov–de Haas measurements. The electrical-transport measurements were performed using a ${}^3\text{He}$ – ${}^4\text{He}$ dilution refrigerator equipped with an 18-T (20-T) superconducting magnet system. For measurements above approximately 10 K, a variable-temperature insert was used, for which data agreed in the overlapping temperature range down to 1.5 K. The sample was contacted electrically by means of wire bonds arranged in a standard six-point Hall configuration. The longitudinal voltage contacts were placed near the edge of the sample. Vanishingly small asymmetries of the longitudinal and transverse voltage pickups under field reversal confirmed essentially perfect contact geometry. Electrical-excitation currents at a frequency of 22.08 Hz were used, in which the absence of Joule heating was confirmed using different excitation amplitudes. The longitudinal and transverse voltage pickups were amplified with impedance-matching transformers selected to match the preamplifiers used. The voltage pickups were recorded simultaneously using digital lock-in detectors. In the dilution refrigerator, the impedance-matching transformer was operated at 1.5 K, reducing the effect of Johnson noise. A piezoelectric rotation stage was used to change the sample orientation *in situ*. The electrical current was applied along the [110] crystallographic direction and the sample was rotated in the (110) plane, perpendicular to the current direction.

For a pedagogical step-by-step illustration of the procedure used to analyse the data, we refer to the supplement of ref. 34. The non-oscillatory signal contributions in ρ_{xy} and ρ_{xx} were approximated by polynomial fits of the fifth and sixth orders, respectively, and subsequently subtracted. Remaining contributions that were not periodic in $1/B$ because of imperfect background subtraction were removed, subtracting a moving average. The QO spectra were confirmed to be insensitive to the precise choice of field range analysed, for which data were recorded up to 20 T for selected temperatures and sample orientations. Spectra shown in our manuscript were analysed for fields between 9 and 18 T. For the Fourier analysis, the data were interpolated at equidistant points in $1/B$. To avoid oversampling, the spacing of the points in $1/B$ corresponded to the spacing at which data were recorded at the highest fields. Between 0 and 1 T⁻¹, extra zeros were added on either side of the range recorded experimentally to enhance the sampling rate of the FFT algorithm (this is known as zero padding). To reduce spectral leakage, a Hamming window was applied before calculating the FFT.

Peaks of the FFT spectra were fitted with Gaussians to determine the oscillation frequencies and amplitudes. Both upsweep and downsweep

of the magnetic field were recorded for each temperature and field orientation and the mean of the oscillation amplitudes and frequencies determined. The variation of the values obtained between upsweeps and downsweeps of the magnetic field was used to estimate the uncertainties of the oscillation frequencies and amplitudes. Effective masses were calculated using the LK temperature reduction factor R_T described in the main text. Uncertainties stated in our paper represent the standard error obtained from the fit. Systematic deviations, for example, arising from the finite field range considered in the analysis, are estimated to be less than 5% of the effective masses inferred from the LK fits.

Nature and concentration of defects. As described in the main text, the magnetic-field dependence of the QOs associated with f_α and f_β correspond to Dingle temperatures of $T_{D\alpha,B} \approx 1.3 \text{ K}$ and $T_{D\beta,B} \approx 1.2 \text{ K}$. A related analysis of the anharmonic content of the QOs yield comparable values of $T_{D\alpha,ah} \approx 0.9 \text{ K}$ and $T_{D\beta,ah} \approx 0.85 \text{ K}$. The associated QPL of the order $\tau_{QP} \approx 10^{-12} \text{ s}$ and Fermi velocity, $v_F \approx 3.4 \times 10^5 \text{ m s}^{-1}$, yield mean free paths of the order $l \approx 3.4 \times 10^{-7} \text{ m}$ (see ref. 36). Given that such tiny defect concentrations change the QO spectra markedly, independent microscopic evidence of the nature and concentration of defects is of great interest.

Unfortunately, there are at present no experimental methods with a suitable sensitivity to provide this information. Adding to the complexity, the QPLs and the Dingle temperatures for different defects may differ by orders of magnitude. Prominent examples reviewed, for example, in the book of Shoenberg²¹ and seminal studies of Springford and collaborators^{53,54} include the mechanical state of the sample (strain), the handling of the sample, as well as imperfections such as dislocations and crystalline mosaicity.

It is, moreover, instructive to comment on the residual resistivity ρ_0 as a probe of the purity of bulk materials used widely. First, ρ_0 reflects the transport lifetime, which is sensitive to large-angle scattering. Hence, to infer the QPL from the resistivity, details of the scattering processes must be known. Second, different types of defect may be present simultaneously, requiring further information on their distribution and interplay. Methods such as remote doping in two-dimensional systems, in which the impurities are physically separated from the conduction channel, are not available in bulk materials. In turn, a direct relationship between the residual resistivity and the Dingle temperature is not expected.

As the Dingle temperature does not distinguish between intraorbit and interorbit contributions, it is essentially not possible to distinguish between different contributions or different types of defects. A possible exception may exist if the Dingle temperatures of the fundamental orbits are similar. In this case, the effects of intraorbit scattering cancel in the ratio of the difference frequency with the second harmonic, thus providing a rough estimate of the interorbit scattering multiplied by a factor reflecting the dimensionality of the system (two dimensions versus three dimensions, for which the three-dimensional system varies with $\sqrt{B/f}$).

DFT calculations. CoSi crystallizes in a simple cubic lattice (SG 198) with both atomic species occupying Wyckoff positions $4a$ with $u_{\text{Co}} = 0.143$ and $u_{\text{Si}} = 0.844$ and experimental lattice constant $a = 4.444 \text{ \AA}$. The band structure and FS were calculated with WIEN2k (ref. 55) and the Vienna Ab initio Simulation Package (VASP) within the generalized gradient approximation by Perdew et al.⁵⁶, taking into account spin-orbit coupling. The bands used to generate FSs were sampled on a $100 \times 100 \times 100$ Monkhorst–Pack grid. Our results are consistent with the reports in the literature^{57,58}.

Predicted QO spectra of Γ -centred FS sheets. An apparent question concerns whether the QO frequencies we attribute to the difference and sum of f_α and f_β are, in fact, due to other FS sheets. Because CoSi

is a semimetal, only FS sheets at the Γ point may be expected, apart from those at the R point. Unfortunately, the experimental detection of QOs arising from the Γ -centred FS sheets of CoSi is incomplete. Although a frequency smaller than 20 T has been reported recently that was attributed to a Γ pocket^{49,50}, the absence of signatures of a larger orbit expected may also be attributed to its large effective masses in conjunction with the quality of the samples available.

As emphasized in the main text, the observation of the same QO frequencies associated with the R point in different samples studied by different groups^{34–36,47–50} establishes the same energy of the electronic bands at the R point. This implies, at high accuracy, a lack of sensitivity of the band structure to defect-induced charge doping. In turn, charge conservation fixes the position of the bands with respect to the Fermi level at the Γ point as follows. Shown in Extended Data Fig. 3a is the calculated band structure around Γ . The value of the Fermi energy E_F of the band structure as calculated is defined to be zero. To satisfy charge conservation, which requires compensation of the hole pockets at R observed experimentally, the bands at the Γ point must be shifted to +7 meV. This adjustment is consistent with the QO oscillation frequency of 20 T attributed to a Γ pocket^{49,50}. It is also consistent with more accurate G_0W_0 calculations⁵⁸.

The FS pockets at the R point observed experimentally in combination with charge conservation fix the Fermi volume at Γ . Ignoring this strong empirical constraint, charge conservation is strongly violated when shifting the bands by ± 20 meV with respect to the point of charge neutrality at +7 meV, as depicted by the grey shading. Namely, when shifting the bands in excess of +20 meV, the characteristic fourfold degeneracy of all FS sheets at Γ shrinks to a point and there are no longer hole-like states. This would imply an electron doping of at least 0.015 electrons per unit cell, which is unrealistically large. On the other hand, shifting the bands by the same magnitude of -20 meV, the resulting position of the Fermi level at -13 meV would yield an even stronger violation of charge neutrality. Thus, for a Fermi value of -1 meV, a hole volume of +3% of the Brillouin zone is already reached, whereas -13 meV corresponds to a hole volume of +5% and thus an unrealistically large hole doping of 0.05.

Marked as coloured horizontal lines are the fictitious positions of the Fermi level when shifting the bands such that a QO frequency of 100 T may exist at all. Two situations may be distinguished. First, when shifting the bands such that $E_F = +17$ meV, shown in Extended Data Fig. 3c, a cross-section of 100 T exists for field along the $\langle 100 \rangle$ directions. However, the frequency varies strongly as a function of field orientation, reaching up to 300 T. Also, the effective mass varies strongly as a function of field direction. Second, when shifting the bands such that $E_F = +1.5$ meV, shown in Extended Data Fig. 3d, a cross-section of 100 T exists for field along the $\langle 100 \rangle$ directions that varies strongly as a function of field orientation, becoming as low as roughly 70 T. Here the effective masses are very large for field along the $\langle 100 \rangle$ directions. Thus, even when strongly violating charge conservation, the FS cross-sections in the vicinity of Γ are in strong contrast with experiment.

Magnetic breakdown. MB between Shubnikov–de Haas orbits around R were evaluated from extremal cross-sections of the FSs using Chambers' formula for the breakdown field

$$B_0 = \frac{\pi\hbar}{2e} \sqrt{\frac{k_g^3}{a+b}}, \quad (3)$$

in which k_g is the gap in k -space and a and b are the curvatures of the trajectories at the breakdown junction^{21,41}. The MB probability at junction j is then given by $p_j = e^{-\frac{B_0}{B}}$, whereas the probability for the charge carrier staying on its trajectory is $q_j = 1 - p_j$. Only breakdown orbits that are closed after one cycle are considered in the analysis. The junctions are found to be in a regime in which breakdown occurs with close to 100% probability for most of the angular range, consistent with the

near crossings dictated by the quasi-symmetries introduced in ref. 36. This results in the simple orbits depicted in grey in Fig. 1d–f, as discussed below.

Combined effect of nodal planes and MB. The way in which the remarkably simple spectrum of only two observable main Shubnikov–de Haas branches arise from the rather intricate FS pockets at the R point has been outlined in Fig. 1 and clarified in detail in refs. 34,36. For the sake of a self-contained discussion, we summarize those results here. In particular, we point out that the two approaches in refs. 34,36,59 are equivalent as long as the MB gaps are small enough to result in a tunnelling probability close to one.

The FS sheets around the R point arise from four interpenetrating bands as shown in Fig. 1b–f. To understand the extremal orbits, one has to consider the band connectivity—governed by the existence of three mutually perpendicular nodal planes—on the one hand and extended regions in which the FS sheets are close enough for MB to occur on the other hand.

In CoSi, all bands are pairwise degenerate on the nodal planes spanning the entire boundary of the simple cubic Brillouin zone. These nodal planes are protected by the joint action of screw rotations and time-reversal symmetry³⁴. The three mutually perpendicular planes intersect at the R point as shown in the upper-left corner of Extended Data Fig. 1a. The band connectivity owing to the nodal planes results in the four FS sheets around R labelled A–D. The FS sheets (C/B) and (A/D) are close to each other in k -space in the breakdown regions marked by coloured circles (bottom), in which almost complete MB occurs. There are no MB junctions between the pairs (A/B) and (C/D), respectively.

The extremal cross-sections of these FS sheets are shown in Extended Data Fig. 1b for three selected planes. In the (001) plane, which is a nodal plane, the bands are doubly degenerate. The band structure in this plane thus corresponds exactly to the minimal scenario of a difference frequency of only two almost parallel bands. This results in two Shubnikov–de Haas orbits (Extended Data Fig. 1c) and the occurrence of difference and sum frequencies induced by interband scattering as discussed in the main text. In the (111) and (110) planes, four different cross-sections exist, with MB junctions marked by coloured circles. Because of complete MB, these result in four orbits with pairwise identical cross-sectional areas as shown in Extended Data Fig. 1c, that is, for all field directions, only two dominant QO frequencies exist.

In ref. 36, a slightly different approach was taken. The authors derived an effective perturbation Hamiltonian around the R point, for which the MB regions between FS sheets were degenerate to the first order in the new Hamiltonian, whereas small gaps appear only at higher orders of the perturbation. The extra surfaces of degeneracy for this approximate first-order Hamiltonian are shown in green in Extended Data Fig. 1d, together with the resulting FS sheets. The corresponding FS sheets are labelled following ref. 36 according to the orbital (1/2) and spin (+/-) degree of freedom. These sheets now intersect on curves in k -space (bottom of Extended Data Fig. 1d) that correspond to the breakdown regions in Extended Data Fig. 1a. The corresponding extremal cross-sections are depicted in Extended Data Fig. 1e. Clearly, they result in the same extremal orbits shown in Extended Data Fig. 1c, without the need to explicitly invoke MB, because the complete MB has already been considered in the construction of the Hamiltonian. The two approaches thus yield consistent results.

Taken together, the nodal planes and MB regions produce a remarkably simple QO spectrum of only two main frequencies. The difference and sum frequencies then arise because of the nonlinear coupling of orbits on these bands.

Inconsistencies with textbook mechanisms of combination frequencies. Before our study, four mechanisms have been reported in the literature that may lead to frequencies in quantum oscillatory

Article

spectra representing linear combinations of fundamental oscillation frequencies. In CoSi, none of these mechanisms allows to account for the properties reported in the manuscript, as explained in the following.

MB represents field-assisted tunnelling of electrons between adjacent orbits in k -space. The only case in which MB can lead to frequencies corresponding to the difference of two basis frequencies is a mixed electron–hole orbit⁶⁰. Because the FS pockets around the R point of CoSi are all electron-like^{34,36}, MB cannot account for the oscillations at $f_{\beta-\alpha}$ observed experimentally. Furthermore, for a mixed electron–hole orbit, one would expect a temperature dependence dictated by the sum of the cyclotron masses of the individual orbits⁵, which is also in strong contrast with our experimental observations.

Magnetic interactions in the context of further QO frequency contributions refers to the feedback of QOs in the magnetization, that is, the de Haas–van Alphen effect, on the internal field. Magnetic interactions may change the QO spectrum and may generate, in principle, a frequency component at $f_{\beta-\alpha}$. A requirement for magnetic interactions to become appreciable is a large amplitude $|dM / dH| \geq 1$ (ref. 21). We have measured the de Haas–van Alphen oscillations of our CoSi sample, in which $|dM / dH|$ is on the order of 10^{-4} , as shown in Extended Data Fig. 5, that is, it is orders of magnitude smaller than required for magnetic interaction. Moreover, oscillation frequencies owing to magnetic interactions are expected to vanish quickly with increasing temperature, in strong contrast to our experimental observations.

QOs of the chemical potential, also known as chemical-potential oscillations, arise when the Landau levels are not coupled to a thermodynamic reservoir. In a multiband metal with several FS pockets, chemical-potential oscillations may lead to a mixing of different oscillation frequencies⁶¹. Chemical-potential oscillations are most pronounced for a (quasi)-two-dimensional FS with only a few Landau levels occupied²¹. In turn, chemical-potential oscillations are well-known in de Haas–van Alphen spectra of (quasi)-two-dimensional materials. In three-dimensional metals, chemical-potential oscillations are suppressed owing to the finite background of unquantized electronic states along the field direction and the joint effect of several FS sheets, which act as a reservoir. As CoSi hosts several three-dimensional Fermi pockets far away from the quantum limit, chemical-potential oscillations will be vanishingly small. Also, no suppression of the temperature dependence of the oscillations is expected for chemical-potential oscillations, in contrast with experiment.

Quantum-interference oscillations, also known as Stark oscillations⁶², may arise from coherent charge-carrier pathways between different MB junctions, that is, they require several MB junctions, and MB probabilities P , with $P(1 - P) \neq 0$. Owing to the interference, the transmission probability of a QP between the two points oscillates with the applied magnetic field. In the case of transport properties, the allowed oscillation frequencies are given by linear combinations of the frequencies associated with the non-interfering trajectories. They may exhibit a very weak thermal damping⁶³. However, in CoSi, for $\parallel [100]$, no MB junctions exist. For other field directions, in which MB junctions are present, the angular evolution of the QO amplitudes³⁴ and quasi-symmetries³⁶ show that $P \approx 1$ for all field directions and MB junctions. Hence, depending on field orientation, the conditions for Stark oscillations in CoSi are either not satisfied or Stark oscillations are strongly suppressed.

Theoretical framework

In the following, we present details of the theoretical framework underlying the formation of QOs of the QPL. The mechanism we consider is a generalization of so-called magneto-intersubband oscillations in two-dimensional electron gases^{32,64–67} and quasi-two-dimensional metals^{33,68,69}. A derivation focusing on technical calculations beyond the scope of the work reported here is presented elsewhere⁷⁰.

Model and conductivity. We use a generic minimal model comprising two rotationally symmetric bands $\lambda = \alpha, \beta$ split in energy. This corresponds to the situation near the R point of CoSi (refs. 34,36). In the following section, we set $\hbar = k_B = 1$.

In the presence of a magnetic field, the electrons are confined to Landau tubes $\varepsilon_\lambda = \omega_{c,\lambda}(l + 1/2) + \frac{k_z}{2m_\lambda} - W_\lambda$ in which $\omega_{c,\lambda} = \frac{eB}{m_\lambda}$ is the band-dependent cyclotron frequency set by the different effective masses m_λ and W_λ is a relative shift in energy. Note, we use the Landau-level dispersion of parabolic bands taking into account the curvature away from the degeneracy point reflecting the experimentally observed band structure. Very similar conclusions are obtained for linearly dispersing bands⁷⁰. Further, we consider randomly distributed short-range impurities by a potential $U(\mathbf{r}) = U_0 \sum_{\mathbf{r}_i} \delta(\mathbf{r} - \mathbf{r}_i)$ with the generic scattering vertex

$$\Lambda = \begin{pmatrix} \Lambda_\alpha & \Lambda_\perp \\ \Lambda_\perp & \Lambda_\beta \end{pmatrix}, \quad (4)$$

in which Λ_α and Λ_\perp denote the strength of the intraband and interband scattering, respectively.

We calculate the conductivity $\hat{\sigma}_{xx}$ at zero temperature using the Kubo formula⁷¹

$$\hat{\sigma}_{xx}(E) = \frac{e^2}{\pi L_x L_y} \text{Tr}_{l,k_x,\lambda,k_z} [\nu_x \text{Im}G(E) \nu_x \text{Im}G(E)], \quad (5)$$

in which $G(E)$ is the retarded, impurity-averaged Green's function $G_{\lambda,l}(E) = (E - \varepsilon_\lambda(l) - \Sigma_\lambda(E))^{-1}$ and ν_x is the velocity operator. Note that, for short-range impurity scattering, the self-energy $\Sigma_\lambda(E)$ does not depend on the Landau level index l .

Evaluation of all sums results in a generic expression for the conductivity kernel⁷⁰,

$$\hat{\sigma}_{xx} = \frac{\sigma_0}{\pi \ell_B} \sum_\lambda \frac{\xi_\lambda^* |\Gamma_\lambda(\xi)|}{1 + 4\Gamma_\lambda(\xi)^2} \left(\frac{2}{3} \sqrt{2\xi_\lambda^*} + \sum_{p=1}^{\infty} \frac{(-1)^p}{\sqrt{p}} \cos\left(2\pi p \xi_\lambda^* - \frac{\pi}{4}\right) R_\lambda(\xi)^p \right), \quad (6)$$

in which ξ_λ^* are the energy-dependent frequencies, $\ell_B = \frac{1}{\sqrt{eB}}$ the magnetic length, $\sigma_0 = 2e^2/\pi$ the unit of conductance and $\Gamma_\lambda = -\text{Im}(\Sigma_\lambda/\omega_{c,\lambda})$ the imaginary part of the dimensionless self-energy, which can be interpreted as the Landau-level broadening (inverse lifetime). In practice, the Landau-level broadening is small compared with the cyclotron frequencies and an expansion in $\Gamma_\lambda \propto 1/\omega_{c,\lambda} \tau_\lambda \ll 1$ recovers the basic formula of the oscillatory component presented in equation (2). The associated damping factor is given by

$$R_\lambda(\xi) = \exp(-2\pi|\Gamma_\lambda(\xi)|). \quad (7)$$

Conventional QOs within LK theory are recovered from the above expression when setting $\text{Im}\Sigma_\lambda$ to a constant, the empirical Dingle temperature $\pi T_{D,\lambda}$, such that $R_\lambda(\xi)$ becomes the well-known Dingle damping factor²¹

$$R_{D,\lambda} = \exp\left(-2\pi^2 \frac{T_{D,\lambda}}{\omega_{c,\lambda}}\right). \quad (8)$$

As our main theoretical result, we go beyond this basic approximation and show that the imaginary part of the self-energy, that is, the band-dependent QPL, $\text{Im}\Sigma_\lambda$, exhibits QOs.

Calculation of the self-energy. We calculate the self-energy in the self-consistent Born approximation by summing the diagonal, irreducible Feynman diagrams up to the second order

$$\Sigma_\lambda = \text{Term 1} + \text{Term 2} + \text{Term 3} \quad (9)$$

in which stars denote the impurities and dots and squares denote, respectively, intraband and interband scattering processes. We note that off-diagonal terms of the self-energy, that is, processes in which the final band index is different from the initial band index, are suppressed by a factor $T_{D,\lambda}/W_1 - W_2 \ll 1$. The last term in the equation represents the relevant interband scattering process coupling the two bands. We may then derive a self-consistent equation for the imaginary part of the self-energy

$$|\text{Im}\Sigma_\lambda(\xi)| = \pi T_{D,\lambda} \left[1 + \tilde{\Lambda}_\lambda^2 \sum_{p=1}^{\infty} \frac{(-1)^p}{\sqrt{2p\xi_\lambda}} \cos(2\pi p \xi_\lambda^*) R_\lambda(\xi)^p + \tilde{\Lambda}_{\perp\lambda}^2 \sum_{p=1}^{\infty} \frac{(-1)^p}{\sqrt{2p\xi_{\perp\lambda}}} \cos(2\pi p \xi_{\perp\lambda}^*) R_{\perp\lambda}(\xi)^p \right], \quad (10)$$

in which $\bar{\lambda}$ represents the other band index with respect to λ . An analogous equation exists for the coupled real part of the self-energy⁷⁰. Note, as $\text{Im}\Sigma_\lambda \propto 1/\tau_\lambda$, we recover equation (1) as the lowest-order solution of equation (10).

Crucially, equation (10) shows that the imaginary part of the self-energy, and hence the QPL, exhibits QOs very similar to the QOs of the conductivity in equation (6) (the tilde labels renormalized quantities). However, as a truly remarkable facet of equation (10), the self-energy of the electrons of a given band, say α , oscillates together with the frequency f_β . These extra oscillations originate from the non-linear interband coupling and result in the emergence of a sum and difference frequency of the conductivity.

QO frequencies and finite temperature behaviour. We solve the self-consistent equation for the self-energy equation (10) by iterative insertion and expansion in orders of the Dingle factor $R_{D,\lambda}$, keeping terms up to the second harmonics. Substituting the result into equation (6), we obtain the conductivity kernel $\hat{\sigma}_{xx}$. The resulting sum consists of summands $\propto \cos(2\pi \frac{f(\xi)}{B})$, in which $f = f_\alpha, f_\beta, 2f_\alpha, 2f_\beta, f_\alpha + f_\beta, f_\beta - f_\alpha$ and more frequencies beyond the second order. Physically, the oscillations with $f_\alpha + f_\beta$ and $f_\beta - f_\alpha$ reflect the interference of the oscillations of the lifetime with the intrinsic oscillations of the conductivity.

We determine the conductivity σ_{xx} at finite temperatures from the conductivity kernel $\hat{\sigma}_{xx}$ by a convolution with the derivative of the Fermi distribution function⁷⁰. The final result reads

$$\begin{aligned} \frac{\sigma_{xx}}{\sigma_0} = & \sum_\lambda A_\lambda \cos\left(2\pi \frac{f_\lambda}{B} - \frac{\pi}{4}\right) R_{D,\lambda} R_T(m_\lambda) \\ & + \sum_\lambda A_{2\lambda} \cos\left(4\pi \frac{f_\lambda}{B} - \frac{\pi}{4}\right) R_{D,\lambda}^2 R_T(2m_\lambda) \\ & + A_{\alpha+\beta} \cos\left(2\pi \frac{f_\alpha + f_\beta}{B} - \frac{\pi}{2}\right) R_{D,\alpha} R_{D,\beta} R_T(m_\alpha + m_\beta) \\ & + A_{\beta-\alpha} \cos\left(2\pi \frac{f_\beta - f_\alpha}{B}\right) R_{D,\alpha} R_{D,\beta} R_T(m_\beta - m_\alpha), \end{aligned} \quad (11)$$

in which the amplitudes A_i only influence the QOs weakly⁷⁰. Notably, we find that $A_{\alpha\pm\beta}/A_\lambda \approx \Lambda_\perp/\Lambda_\lambda (1/\sqrt{f_\alpha} + 1/\sqrt{f_\beta})$, leading to the conclusion that, even if the amplitude of the difference frequency is small, interband coupling can be strong; see Extended Data Fig. 7. Note that the difference and sum of the frequencies are damped with the sum of the

Dingle temperatures of the fundamental oscillation frequencies. By contrast, the decay in temperature, set by R_T , is governed by the difference or the sum of the effective masses of the fundamental frequencies. Furthermore, the sum and the difference frequency inherit the phases of the fundamental frequencies, that is, the phases of the combination frequencies are $\varphi_{\beta\pm\alpha} = \varphi_\beta \pm \varphi_\alpha$, which provides another experimental test permitting their identification.

Interband coupling from magnetic impurity scattering. The interband impurity scattering contribution is key for observing difference frequency QOs. In the following, we evaluate how the underlying spin-1 multifold fermion excitation may be responsible for the strong interband impurity scattering channels. CoSi belongs to SG198, for which excitations around R can be described by a generic low-energy $\mathbf{k} \cdot \mathbf{p}$ theory^{58,72,73}. The band structure features a spin-1 multifold fermion, which forms out of two Weyl nodes because of spin-orbit coupling. The $\mathbf{k} \cdot \mathbf{p}$ Hamiltonian (\mathbf{k} is the momentum with respect to the R point) reads

$$H_R = v \mathbb{1} \otimes \mathbf{k} \cdot \boldsymbol{\sigma} + \frac{\Delta}{4} (\sigma_x \otimes \sigma_x + \sigma_y \otimes \sigma_y + \sigma_z \otimes \sigma_z), \quad (12)$$

in which σ_i are the Pauli matrices and, for CoSi, $v \approx -1.3$ eV and $\Delta \approx 31$ meV, is known to be an effective description along the surface of the Brillouin zone⁵⁸. Equation (12) is denoted in the orbital basis in which the first index is spin s and the second is pseudospin τ related to the sublattice structure. We denote the bands $E_{\alpha_k} = v|\mathbf{k}| + \frac{\Delta}{4}$, $E_{\beta_k} = -\frac{\Delta}{4} + \sqrt{\left(\frac{\Delta}{2}\right)^2 + v^2 \mathbf{k}^2}$ of the low-energy Hamiltonian by $|\lambda\rangle$, in which $|\alpha_k\rangle$ and $|\beta_k\rangle$ are the two relevant bands for the observed QOs, as they set the frequencies (see Extended Data Fig. 7). Notably, the electron spin in the band α (β) is polarized antiparallel (parallel) to its momentum, consistent with CoSi (ref. 36).

We consider simple potential impurities that are distributed uniformly over the system. The simplest and most common form of impurity potentials is diagonal in the orbital basis $\Lambda = \sum_{s,\eta} \Lambda_{s,\eta} |s, \eta\rangle \langle s, \eta|$ but dependent on spin and pseudospin. By using the analytic expressions for the band eigenstates, we can then show that the interband coupling $\Lambda_\perp = \langle \alpha_k | \Lambda | \beta_k \rangle \propto \sum_\eta (\Lambda_{\downarrow,\eta} - \Lambda_{\uparrow,\eta})$ is substantial if the scattering breaks time-reversal symmetry.

In the case of CoSi, it has been known for a long time that impurities lead to local moment formation on the Co atoms, for example, for Fe impurities in the crystal^{74–77}. These time-reversal-symmetry-breaking impurities then directly imply different signs for $\Lambda_{\uparrow,\eta}$ and $\Lambda_{\downarrow,\eta}$, hence, they already lead, at the basic level of potential impurity scattering in the orbital basis, to a finite interband coupling.

Note that the fact that the amplitudes of the difference and sum frequency are much smaller than the amplitudes of the ordinary second harmonics does not imply that $\Lambda_\perp \ll \Lambda_\alpha$. QOs of the lifetime come with a different prefactor, leading to a smaller contribution to the total spectrum in three dimensions. In fact, the measured QO spectrum in CoSi suggests that interband and intraband scattering are roughly equally strong, increasing the importance of the interband scattering mechanism.

Taken together, we argue that the universal band structure related to the multifold spin-1 fermions in CoSi together with magnetic impurities may give rise to an effective interband coupling that accounts for the observation of QOs of the QPL.

Data availability

Data reported in this paper are available at <https://doi.org/10.5281/zenodo.7957067>.

46. Yuan, Q.-Q. et al. Quasiparticle interference evidence of the topological Fermi arc states in chiral fermionic semimetal CoSi. *Sci. Adv.* **5**, eaaw9485 (2019).
47. Wu, D. S. et al. Single crystal growth and magnetoresistivity of topological semimetal CoSi. *Chin. Phys. Lett.* **36**, 077102 (2019).

Article

48. Xu, X. et al. Crystal growth and quantum oscillations in the topological chiral semimetal CoSi. *Phys. Rev. B* **100**, 045104 (2019).
49. Wang, H. et al. de Haas-van Alphen quantum oscillations and electronic structure in the large-Chern-number topological chiral semimetal CoSi. *Phys. Rev. B* **102**, 115129 (2020).
50. Sasnal, S. et al. Shubnikov-de Haas and de Haas-van Alphen oscillations in Czochralski grown CoSi single crystal. *J. Phys. Condens. Matter* **34**, 425702 (2022).
51. Neubauer, A. et al. Ultra-high vacuum compatible image furnace. *Rev. Sci. Instrum.* **82**, 013902 (2011).
52. Bauer, A., Benka, G., Regnat, A., Franz, C. & Pfleiderer, C. Ultra-high vacuum compatible preparation chain for intermetallic compounds. *Rev. Sci. Instrum.* **87**, 113902 (2016).
53. Springford, M. The anisotropy of conduction electron scattering in the noble metals. *Adv. Phys.* **20**, 493–550 (1971).
54. Paul, D. M. & Springford, M. Accurate measurement of changes in electron scattering in the de Haas-van Alphen effect. *J. Low Temp. Phys.* **27**, 561–569 (1977).
55. Blaha, P. et al. WIEN2k: an APW+lo program for calculating the properties of solids. *J. Chem. Phys.* **152**, 074101 (2020).
56. Perdew, J. P., Burke, K. & Ernzerhof, M. Generalized gradient approximation made simple. *Phys. Rev. Lett.* **77**, 3865–3868 (1996).
57. Tang, P., Zhou, Q. & Zhang, S.-C. Multiple types of topological fermions in transition metal silicides. *Phys. Rev. Lett.* **119**, 206402 (2017).
58. Pshenay-Severin, D. A., Ivanov, Y. V., Burkov, A. A. & Burkov, A. T. Band structure and unconventional electronic topology of CoSi. *J. Phys. Condens. Matter* **30**, 135501 (2018).
59. Wilde, M. & Pfleiderer, C. Large curvature near a small gap. *Nat. Phys.* **18**, 731–732 (2022).
60. O'Brien, T. E., Diez, M. & Beenakker, C. W. J. Magnetic breakdown and Klein tunneling in a type-II Weyl semimetal. *Phys. Rev. Lett.* **116**, 236401 (2016).
61. Alexandrov, A. S. & Bratkovsky, A. M. New fundamental dHvA frequency in canonical low-dimensional Fermi liquids. *Phys. Lett. A* **234**, 53–58 (1997).
62. Stark, R. W. & Friedberg, C. B. Quantum interference of electron waves in a normal metal. *Phys. Rev. Lett.* **26**, 556–559 (1971).
63. Kaganov, M. I. & Slutskin, A. A. Coherent magnetic breakdown. *Phys. Rep.* **98**, 189–271 (1983).
64. Leadley, D. R. et al. Intersubband resonant scattering in GaAs-Ga_{1-x}Al_xAs heterojunctions. *Phys. Rev. B* **46**, 12439–12447 (1992).
65. Coleridge, P. T. Inter-subband scattering in a 2D electron gas. *Semicond. Sci. Technol.* **5**, 961–966 (1990).
66. Raikh, M. E. & Shahbazyan, T. V. Magnetointersubband oscillations of conductivity in a two-dimensional electronic system. *Phys. Rev. B* **49**, 5531–5540 (1994).
67. Goran, A. V., Bykov, A. A., Toropov, A. I. & Vitkalov, S. A. Effect of electron-electron scattering on magnetointersubband resistance oscillations of two-dimensional electrons in GaAs quantum wells. *Phys. Rev. B* **80**, 193305 (2009).
68. Grigoriev, P. D. Theory of the Shubnikov-de Haas effect in quasi-two-dimensional metals. *Phys. Rev. B* **67**, 144401 (2003).
69. Thomas, I. O., Kabanov, V. V. & Alexandrov, A. S. Shubnikov-de Haas effect in multiband quasi-two-dimensional metals. *Phys. Rev. B* **77**, 075434 (2008).
70. Leeb, V. & Knolle, J. On the theory of difference frequency quantum oscillations. Preprint at <https://arxiv.org/abs/2306.10760> (2023).
71. Bastin, A., Lewiner, C., Betbeder-matibet, O. & Nozieres, P. Quantum oscillations of the Hall effect of a Fermion gas with random impurity scattering. *J. Phys. Chem. Solids* **32**, 1811–1824 (1971).
72. Mañes, J. L. Existence of bulk chiral fermions and crystal symmetry. *Phys. Rev. B* **85**, 155118 (2012).
73. Bradlyn, B. et al. Beyond Dirac and Weyl fermions: unconventional quasiparticles in conventional crystals. *Science* **353**, aaf5037 (2016).
74. Yasuoka, H., Sherwood, R., Wernick, J. & Wertheim, G. Local moment formation in substituted and cobalt-rich CoSi. *Mater. Res. Bull.* **9**, 223–231 (1974).
75. Wernick, J., Wertheim, G. & Sherwood, R. Magnetic behavior of the monosilicides of the 3d-transition elements. *Mater. Res. Bull.* **7**, 1431–1441 (1972).
76. Wertheim, G. K., Wernick, J. H. & Buchanan, D. N. E. Mössbauer effect in Co_{1-x}Fe_xSi. *J. Appl. Phys.* **37**, 3333–3337 (1966).
77. Kawarasaki, S., Yasuoka, H. & Nakamura, Y. Moment formation on Co atom in FeSi-CoSi mixed system -Co⁵⁹ NMR in the paramagnetic state. *Solid State Commun.* **10**, 919–921 (1972).

Acknowledgements We wish to thank A. Schnyder for discussions. J.K. acknowledges helpful discussions with N. R. Cooper. V.L. acknowledges support from the Studienstiftung des deutschen Volkes. N.H. and V.L. acknowledge support from the TUM Graduate School. M.A.W. and C.P. acknowledge support by the Deutsche Forschungsgemeinschaft (DFG, German Research Foundation) - TRR 80 - 107745057; TRR 360 - 492547816 and DFG-CACR project WI3320/3 - 323760292. C.P. acknowledges support through DFG SPP 2137 (Skyrmionics) under grant no. PF393/19 (project ID 403191981), ERC Advanced Grant no. 788031 (ExQuSiD) and Germany's excellence strategy under EXC-2111390814868. J.K. acknowledges support from the Imperial-TUM flagship partnership. This research is part of the Munich Quantum Valley, which is supported by the Bavarian State Government with funds from the Hightech Agenda Bayern Plus.

Author contributions M.A.W. and C.P. conceived and started this study. M.A.W., C.P. and J.K. proposed the interpretation. G.B. and A.B. prepared and characterized the samples. N.H. conducted the measurements and analysed the data. M.A.W. and V.L. performed band-structure calculations. M.A.W. and N.H. connected the experimental data with the calculated band structure. V.L. and J.K. developed the theoretical analysis. C.P., M.A.W. and J.K. wrote the manuscript, with contributions from N.H. and V.L. All authors discussed the data and commented on the manuscript.

Competing interests The authors declare no competing interests.

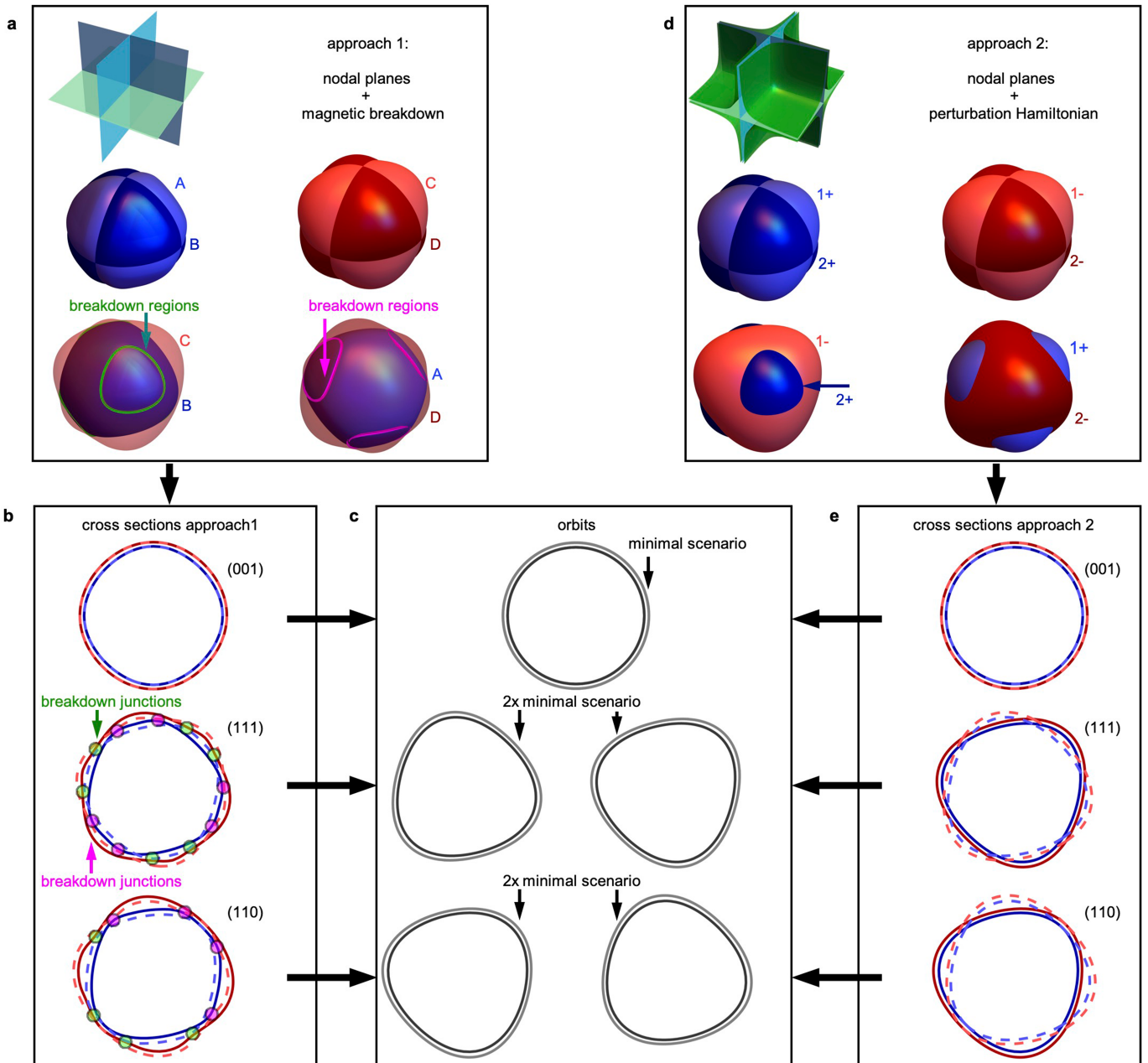
Additional information

Supplementary information The online version contains supplementary material available at <https://doi.org/10.1038/s41586-023-06330-y>.

Correspondence and requests for materials should be addressed to Johannes Knolle, Christian Pfleiderer or Marc A. Wilde.

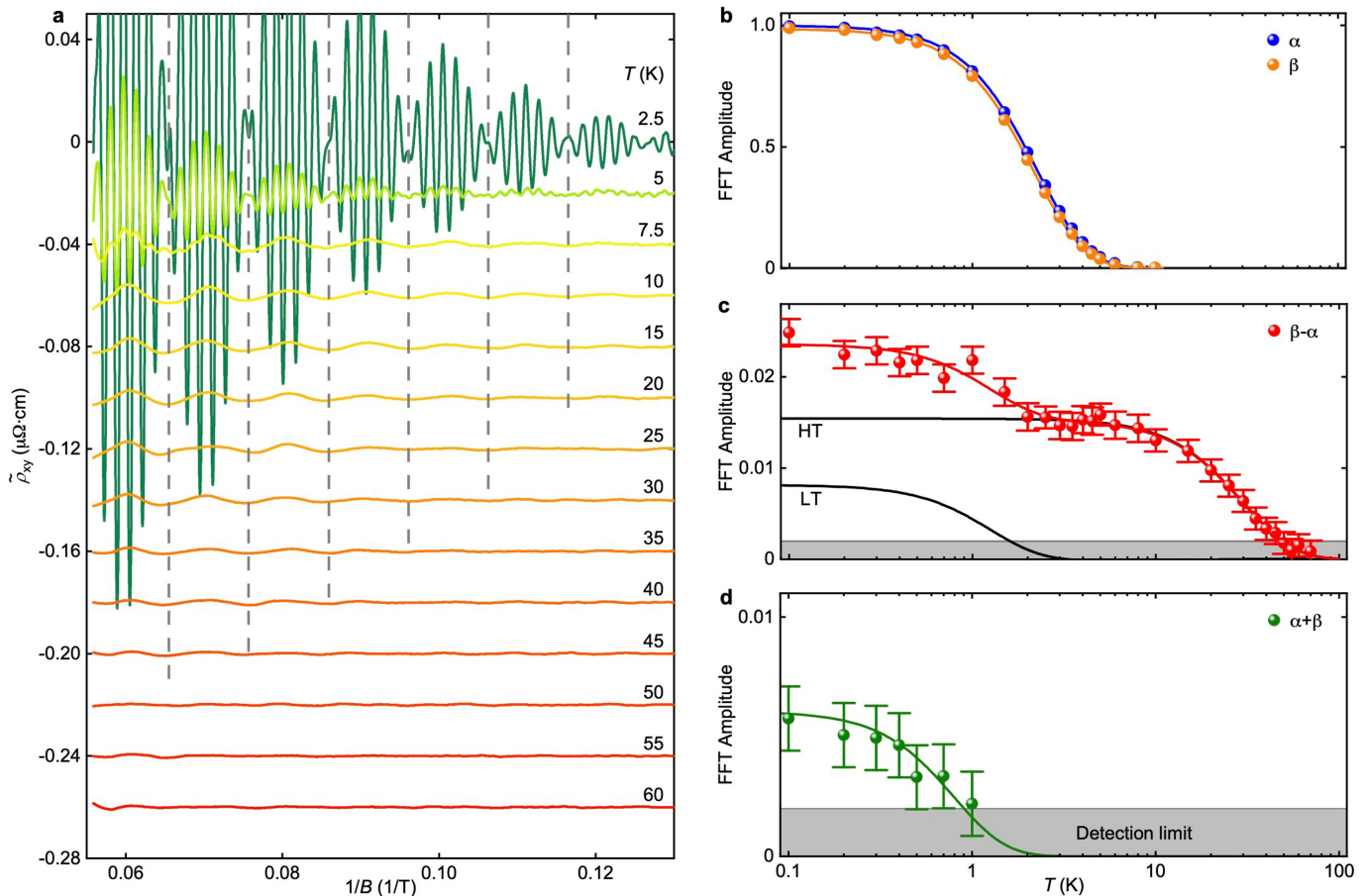
Peer review information *Nature* thanks Luis Balicas, Zhi-Ming Yu and the other, anonymous, reviewer(s) for their contribution to the peer review of this work. Peer reviewer reports are available.

Reprints and permissions information is available at <http://www.nature.com/reprints>.



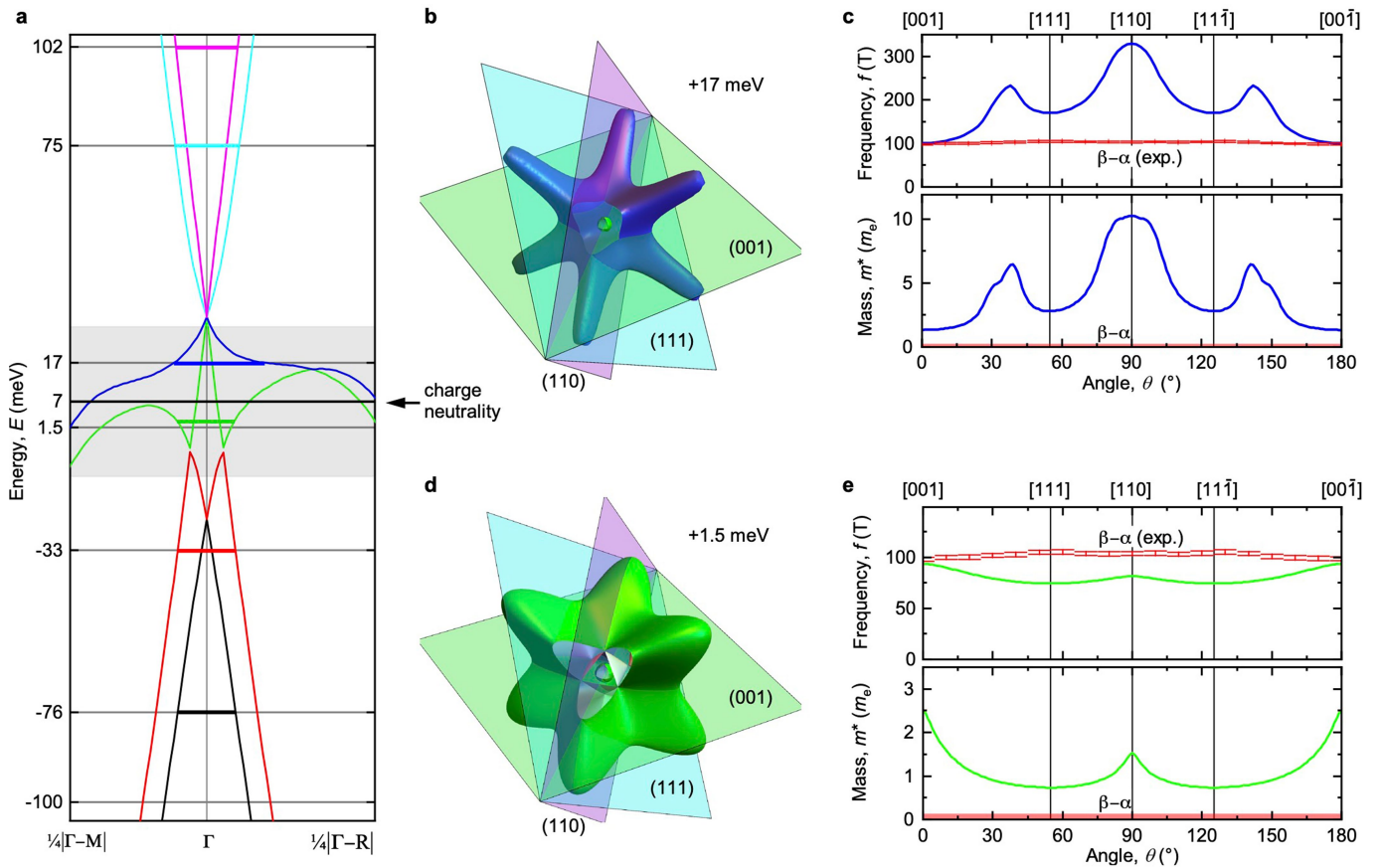
Extended Data Fig. 1 | Equivalence of predicted QO orbits when invoking MB (ref. 34) or hidden quasi-symmetries (ref. 36). Panels are organized in the spirit of a flow chart. **a**, Approach 1 comprises nodal planes and MB³⁴. Three mutually perpendicular nodal planes at the R point as depicted at the top of the panel enforce pairwise band degeneracies of the FS sheets labelled A, B and C, D. Numerically calculated MB with probabilities close to 1 occur between sheet pairs (C,B) and (A,D) along the lines as marked. **b**, Extremal cross-section for the three selected planes. In the (001) plane, the cross-sections are doubly degenerate. In the (111) and (110) planes, four different cross-sections exist, with MB junctions denoted by coloured circles. The cross-sectional areas are always pairwise identical. **c**, Effective extremal orbits corresponding to panels **b** and **e**. For all field directions, two dominant QO frequencies exist. **d**, Approach 2 comprises nodal planes and hidden quasi-symmetries³⁶.

Three mutually perpendicular nodal planes at the R point are enclosed by regimes of hidden quasi-symmetry up to the enclosing surfaces (green), as depicted at the top of the panel. Within the green regimes, near degeneracies are approximated by exact degeneracies in first-order perturbation theory. The FS sheets of the perturbation Hamiltonian are labelled as orbital (1/2) and spin (+/-) degrees of freedom, for which sheet pairs (1-/2+) and (1+/2-) intersect at the surfaces of the quasi-symmetry. **e**, Extremal cross-sections for the same three selected planes shown in **b**. In the (001) plane, the cross-sections are doubly degenerate, identical to **b**. In the (111) and (110) planes, the cross-sections correspond to the extremal orbits as depicted in **b** with breakdown gaps that approach zero. Taken together, approaches 1 and 2 yield the same orbits as depicted in **c** and thus the same two QO frequencies.



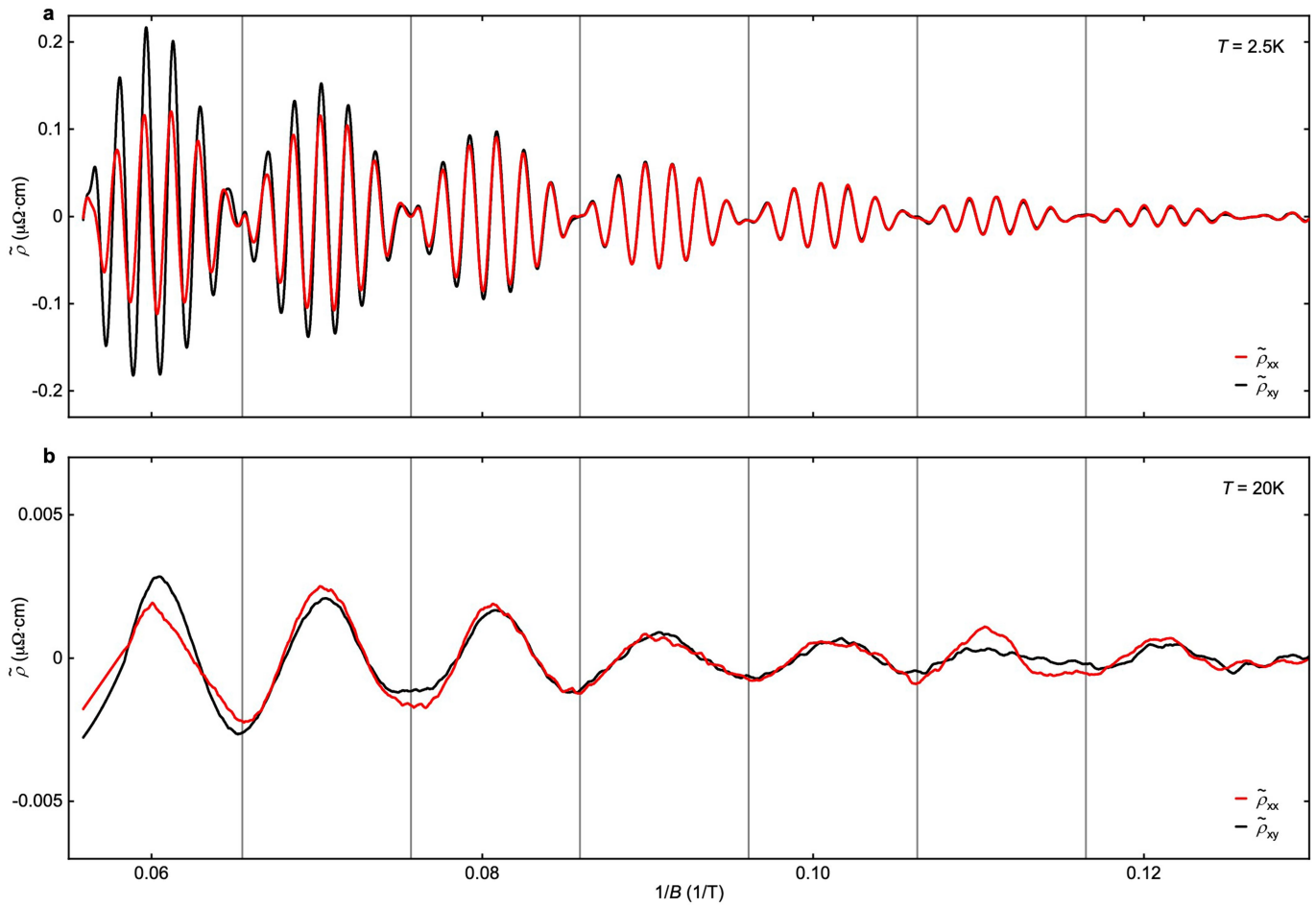
Extended Data Fig. 2 | Temperature dependence of Shubnikov-de Haas oscillations in the Hall resistivity of CoSi. Oscillation amplitudes shown in panels **b–d** were analysed in the magnetic field range between 9 and 18 T with \mathbf{B} applied along the [001] direction and normalized to the amplitude of f_α at $T = 20$ mK. **a**, Oscillatory component of ρ_{xy} as a function of inverse magnetic field at different temperatures. Curves are shifted by a constant. **b**, Oscillation amplitudes of the α and β frequencies. Lines represent a fit with the temperature reduction factor R_T in the LK formalism. Effective masses inferred from the fit are $m_\alpha^* = (0.92 \pm 0.01)m_e$ and $m_\beta^* = (0.95 \pm 0.01)m_e$. Error bars are

smaller than the data points. **c**, Oscillation amplitudes of the difference frequency $f_{\beta-\alpha}$. The red line represents a two-component fit of the temperature reduction factor, yielding effective masses of $(0.07 \pm 0.01)m_e$ and $(1.6 \pm 0.3)m_e$, corresponding to the difference and the sum of the individual masses within the error bars and consistent with the QPL oscillations reported in this work. The black lines represent the individual components of the fit, in which HT and LT denote the high-temperature and low-temperature behaviour, respectively. **d**, Amplitude of the sum frequency $f_{\alpha+\beta}$. The line represents a LK fit yielding a cyclotron mass of $(2.6 \pm 0.4)m_e$.



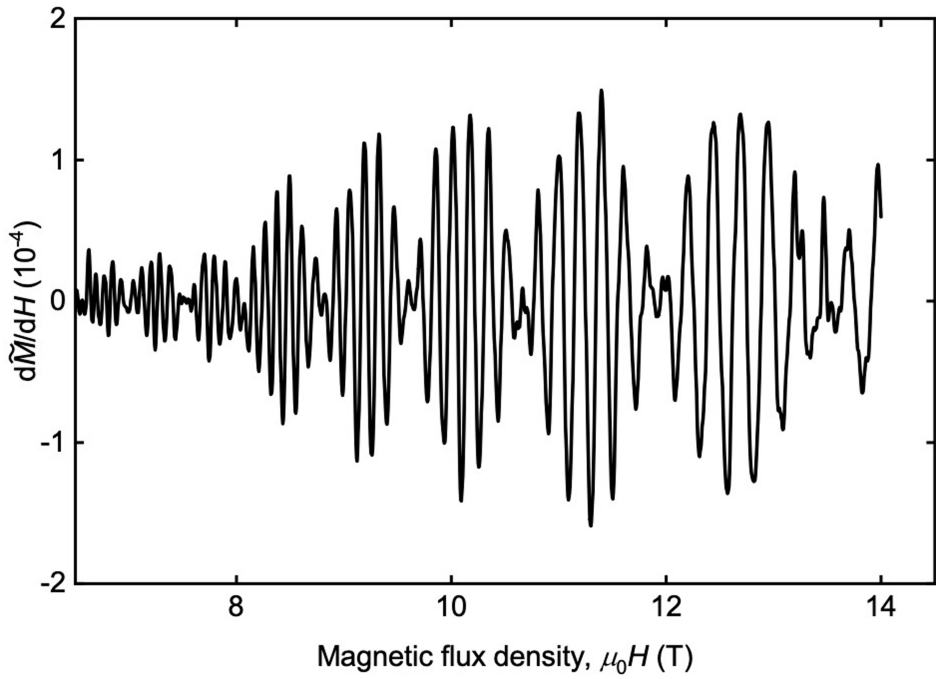
Extended Data Fig. 3 | Calculated FS orbits near the Γ point of CoSi under various conditions. The observation of essentially identical values of f_α and f_β in different samples studied by different groups^{34,36,47–50} establishes the same energy of the electronic bands at the R point and thus a lack of sensitivity of the band structure to defect-induced charge doping. In turn, charge conservation enforces a position of the bands with respect to the Fermi level at the Γ point within 1 meV. No QO frequencies of around 100 T are expected under these conditions. **a**, Calculated band structure in the vicinity of the Γ point of CoSi. For the FS pockets at the R point observed experimentally, a value of $E_F = (+7 \pm 1)$ meV at the Γ point, marked by the black horizontal line, corresponds to charge neutrality. The grey shading depicts a range of ± 20 meV beyond which hole carriers vanish altogether and charge conservation would be violated substantially (see Methods for details). Coloured horizontal lines at $E_F = +17$ meV and $E_F = +1.5$ meV denote locations in which FS cross-sections with QO frequencies of around 100 T are expected, but for $\mathbf{B} \parallel \langle 001 \rangle$ only. **b**, FS sheets

centred at Γ for $E_F = +17$ meV, in which the sheets depicted in blue and green shading correspond to the blue and green bands shown in panel **a**. **c**, Upper panel, calculated angular dispersion $f(\theta)$ of the blue band for $E_F = +17$ meV as compared with the experimental data (red symbols) shown in Fig. 2i. Lower panel, calculated dispersion of the cyclotron mass (blue) as compared with the experimental value (red), at which strong disagreement would be expected. QOs with a frequency of around 100 T are expected for $\mathbf{B} \parallel \langle 001 \rangle$ only, in which the predicted mass differs strongly from experiment. **d**, Green FS sheet centred at Γ for $E_F = +1.5$ meV. **e**, Upper panel, calculated angular dispersion $f(\theta)$ of the green band for $E_F = +1.5$ meV as compared with the experimental data (red symbols) shown in Fig. 2i. Lower panel, calculated dispersion of the cyclotron mass (green) as compared with the experimental value (red), in which strong disagreement would be expected. QOs with a frequency of around 100 T are expected for $\mathbf{B} \parallel \langle 001 \rangle$ only, in which the predicted mass differs strongly from experiment.



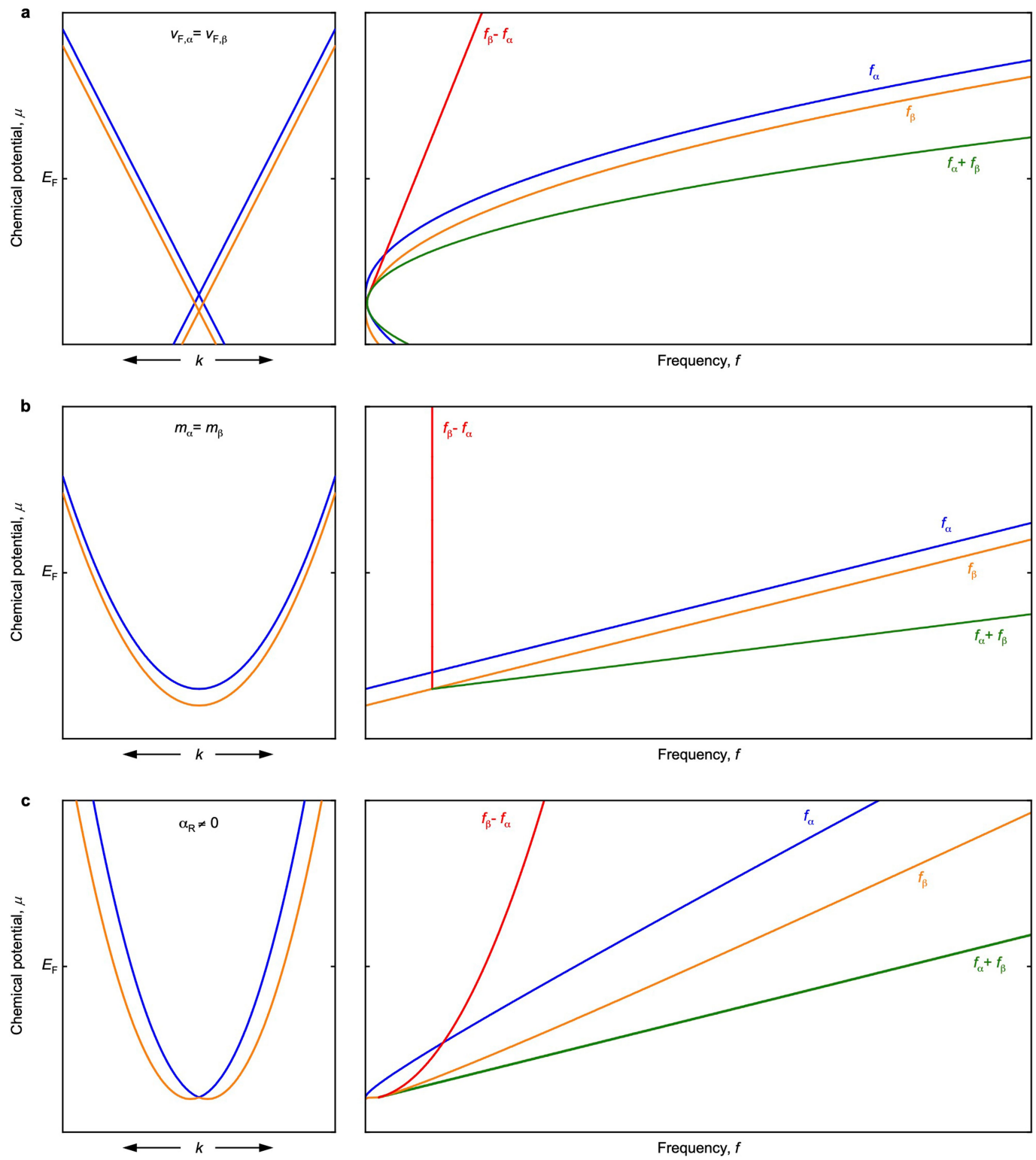
Extended Data Fig. 4 | Analysis of the phase relation between the Shubnikov-de Haas oscillations at different temperatures. **a**, Oscillatory component of the transverse magnetoresistivity, $\tilde{\rho}_{xx}$, and Hall resistivity, $\tilde{\rho}_{xy}$, as a function of inverse magnetic field at $T=2.5\text{ K}$. A pronounced beating pattern originates from oscillations at f_a and f_β . Nodes of the beating pattern are indicated by vertical lines. The envelope of the beating pattern may be expressed as $\cos(2\pi(f_\beta-f_a)/(2B) + (\varphi_\beta-\varphi_a)/2)$, in which φ_a and φ_β are the phases off f_a and f_β , respectively. An analysis using the frequencies determined from the FFT peaks, notably $f_a=565\text{ T}$ and $f_\beta=663\text{ T}$, yields a phase difference of

$\varphi_\beta-\varphi_a=0.16\pi$. We note that this value sensitively depends on the precise value of the frequency difference $f_\beta-f_a$. **b**, Oscillatory component of the resistivities as a function of inverse applied magnetic field at $T=20\text{ K}$. The oscillations at f_a and f_β are strongly suppressed at this temperature. Only the slow oscillations at $f_{\beta-a}$ are visible. Here minima of the oscillations coincide with the nodes of the beating pattern shown in panel **a**. Neglecting the amplitude, the oscillation at $f_{\beta-a}$ may be described by a term reading $\cos(2\pi f_{\beta-a}/B + \varphi_{\beta-a})$, which oscillates with the same frequency as the nodes in the beating pattern. The phase $\varphi_{\beta-a}$ matches the phase difference $\varphi_\beta-\varphi_a$.



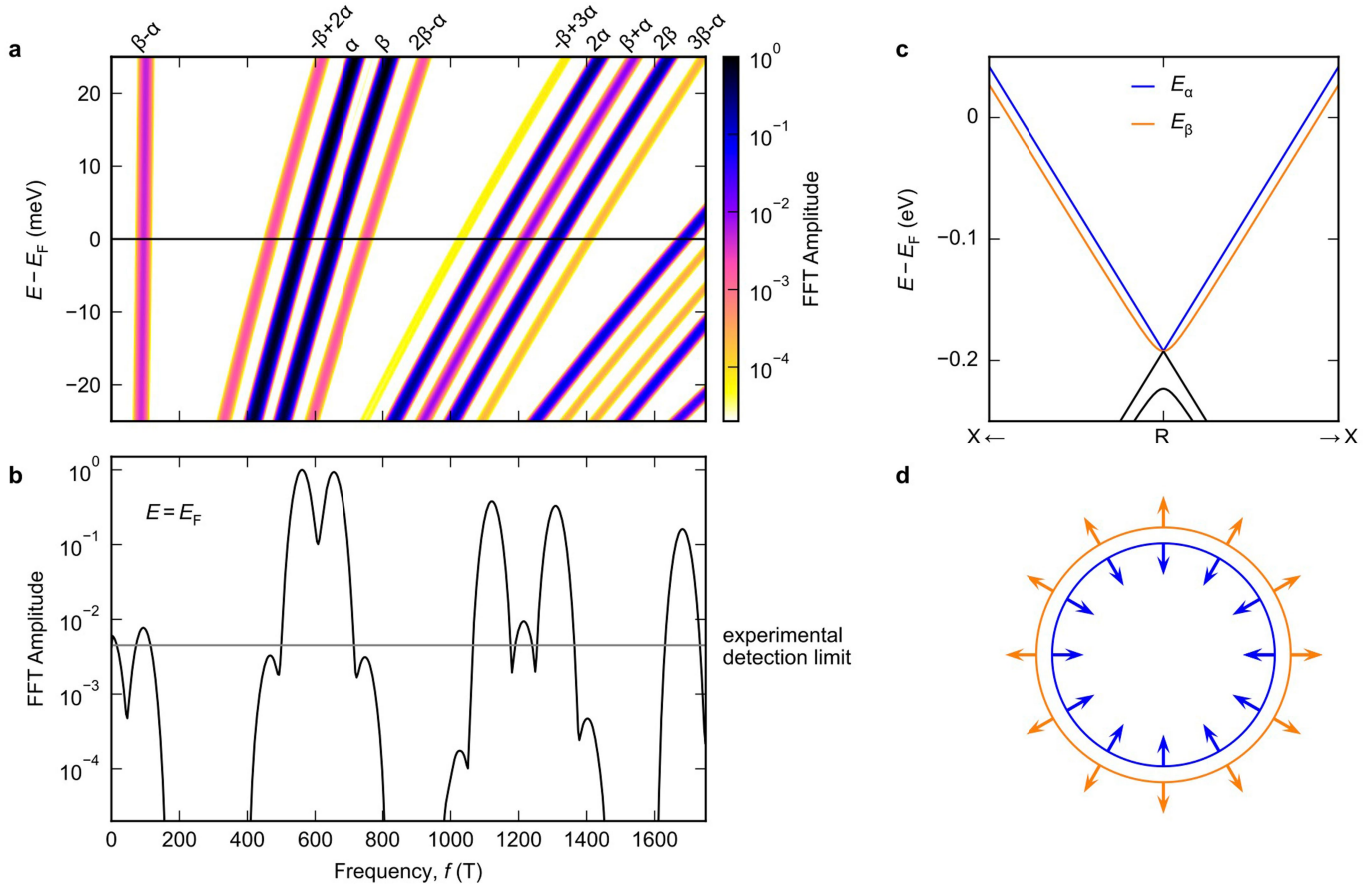
Extended Data Fig. 5 | Quantitative assessment of the effects of magnetic interactions in CoSi. Changes of the magnetization owing to de Haas–van Alphen oscillations may generate variations of the internal field that result in oscillatory signal components observed in the physical properties. This feedback is known as magnetic interaction. Shown is the derivative of the oscillatory part of the measured magnetization in SI units as a function of applied magnetic field. For contributions on the order $d\tilde{M}/dH \approx 1$, oscillatory

signal contributions owing to magnetic interactions are commonly expected²¹. The de Haas–van Alphen contribution observed experimentally is well below this limit. Numerical simulations of the effect of magnetic interactions expected in our study establish that the amplitudes of the de Haas–van Alphen oscillations at f_x and f_y are several orders of magnitude below the value required to account for the oscillatory signal components at the difference of the frequencies we observed experimentally.



Extended Data Fig. 6 | Characteristic frequencies of QOs of the QPL for generic types of band pair. Precondition for QOs of the QPL is a general form of interaction, such as scattering from defects or collective excitations, that generate a nonlinear intraorbit or interorbit coupling. **a.** Left, two linear bands with equal Fermi velocities, $v_{F,\alpha} = v_{F,\beta}$, and a small offset. This configuration may be expected near multifold band crossings as in CoSi. The crossings need not be topological. Right, the small variation of $f_\beta - f_\alpha$ owing to the band offset leads to a strongly reduced suppression of the dephasing of the oscillation amplitude

as a function of temperature. **b.** Left, parabolic bands with equal masses, $m_\alpha = m_\beta$, and a small offset. Right, the difference frequency $f_\beta - f_\alpha$ is independent of the Fermi level, as the cyclotron masses are equal. The dephasing as a function of temperature and hence the decay of the oscillation amplitude with increasing temperature is suppressed completely. **c.** Left, Rashba-type spin-orbit splitting, in which the Rashba parameter $\alpha_R \neq 0$. Right, the temperature dephasing depends on E_F , as the slope of $f_\beta - f_\alpha$ is not constant.



Extended Data Fig. 7 | Predicted QO spectra and possible mechanism of interband scattering. The dependence of the QO frequencies on energy is key to understanding their temperature dependence. **a**, FFT amplitude of equation (11) over an extended B -field range at $T = 0$. As well as equation (11), leading contributions up to the fourth order in the Dingle factor are included, which can be evaluated systematically. Experimental values for m_A^* and $T_{D,A} \approx 0.5$ K were used consistent with CoSi, as well as $f_\alpha(E), f_\beta(E)$ from the DFT calculations. **b**, Cut along $E = E_F$ for CoSi. This may be compared with the

spectrum recorded experimentally. Peaks shown in panels **a** and **b** seem broad because of the log scale. **c**, Band structure of the effective $\mathbf{k} \cdot \mathbf{p}$ Hamiltonian around the R point equation (12) used to model a possible mechanism for nonlinear interband scattering. **d**, Schematic FSs in the effective $\mathbf{k} \cdot \mathbf{p}$ Hamiltonian (projection on the $k_z = 0$ plane with respect to R) in which the spin is polarized perpendicular to the FS and orientated in opposing directions on the two bands. This is consistent with results obtained in DFT calculations³⁶.